DISSERTATIONES
CHIMICAE
UNIVERSITATIS
TARTUENSIS
212

ALAR HEINSAAR

Investigation of oxygen electrode materials for high-temperature solid oxide cells in natural conditions

DISSERTATIONES CHIMICAE UNIVERSITATIS TARTUENSIS
212

DISSERTATIONES CHIMICAE UNIVERSITATIS TARTUENSIS
212

ALAR HEINSAAR

Investigation of oxygen electrode materials for high-temperature solid oxide cells in natural conditions

UNIVERSITY OF TARTU
Press
1632

Institute of Chemistry, Faculty of Science and Technology, University of Tartu, Estonia

The dissertation is accepted for the commencement of the degree of Doctor of Philosophy in Chemistry on June 17th, 2022, by the Council of Institute of Chemistry, University of Tartu.

Supervisors:	Ph.D. Indrek Kivi University of Tartu, Estonia
	Prof. Enn Lust University of Tartu, Estonia
Opponent:	Prof. Søren Højgaard Jensen Aalborg University The Faculty of Engineering and Science, Denmark Energy Storage Consultant, DynElectro ApS
Commencement:	17.08.2022, at 12:15. Auditorium 1020, Ravila 14a, Tartu

European Union
European Regional
Development Fund

Investing
in your future

ISSN 1406-0299
ISBN 978-9949-03-947-0 (print)
ISBN 978-9949-03-948-7 (pdf)

University of Tartu Press
www.tyk.ee

TABLE OF CONTENTS

1. LIST OF ORIGINAL PUBLICATIONS

I. I. Kivi, J. Aruväli, K. Kirsimäe, A. Heinsaar, G. Nurk, E. Lust, Oxygen stoichiometry in $La_{0.6}Sr_{0.4}CoO_{3-\delta}$ and $La_{0.6}Sr_{0.4}Co_{0.2}Fe_{0.8}O_{3-\delta}$ cathodes under applied potential as a function of temperature and oxygen partial pressure, measured by novel electrochemical in situ high-temperature XRD method, J. Electrochem. Soc. 160 (9) (2013) F1022–F1026.

II. I. Kivi, J. Aruväli, K. Kirsimäe, A. Heinsaar, G. Nurk, E. Lust, Kinetic response of La0.6Sr0.4CoO3-d lattice parameters to electric potential change in porous cathode at in situ solid oxide fuel cell conditions, J. Electrochem. Soc. 162 (3) (2015) F354–F358.

III. I. Kivi, J. Aruväli, K. Kirsimäe, P. Möller, A. Heinsaar, G. Nurk, E. Lust, Influence of humidified synthetic air feeding conditions on the stoichiometry of $(La_{1-x}Sr_x)_yCoO_{3-\delta}$ and $La_{0.6}Sr_{0.4}Co_{0.2}Fe_{0.8}O_{3-\delta}$ cathodes under applied potential measured by electrochemical in situ high-temperature XRD method, J. Solid State Electrochemistry 21 (2) (2017) 361–369.

IV. A. Heinsaar, I. Kivi, P. Möller, K. Kooser, T. Käämbre, J. Aruväli, G. Nurk, E. Lust, Influence of Carbon Dioxide and Humidity on the Stability of $(La_{0.6}Sr_{0.4})_{0.99}Co_{1-x}Ti_xO_{3-\delta}$ Cathode, J. Electrochem. Soc. 169 (1) (2022) 014514.

Author's contribution:

Paper I: Performed the synthesis of single cells, therewith some physical and all electrochemical characterization of the single cells and data analysis.

Paper II: Performed the synthesis of single cells, therewith some physical and all electrochemical characterization of the single cells and data analysis.

Paper III: Performed the synthesis of the single cells, therewith all physical and all electrochemical characterization of the single cells and data analysis.

Paper IV: Performed the synthesis of the single cells, therewith some physical and all electrochemical characterization of the single cells and analysis of the data. Mainly responsible for the preparation of the manuscript.

2. ABBREVIATIONS AND SYMBOLS

a	crystallographic parameter
AC	alternating current
c	crystallographic parameter
C	capacitance
CE	counter electrode
CPE	constant phase element
D	the mean or actual crystallite size
d	the distance between lattice planes
DC	direct current
DRT	the distribution of relaxation times
E	electrode potential
EC	equivalent circuit
EIS	Electrochemical impedance spectroscopy
f	frequency
g_τ	*the* relative contribution of the single process to the total polarization resistance
GDC	$Ce_{0.9}Gd_{0.1}O_{2-\delta}$
FC	fuel cell
FWHM	full width at half maximum
h_τ	the total contribution of the single process to the total polarization resistance
I_0	amplitude of the current
$I(t)$	alternating current function on time
K	Scherrer constant
λ	the wavelength of the X-ray
L	inductance
LSC	$La_{0.6}Sr_{0.4}CoO_{3-\delta}$
LSC + LSCF	$La_{0.6}Sr_{0.4}CoO_{3-\delta}$ + $La_{0.6}Sr_{0.4}Co_{0.2}Fe_{0.8}O_{3-\delta}$
LSC99	$(La_{0.6}Sr_{0.4})_{0.99}CoO_{3-\delta}$
LSC101	$(La_{0.6}Sr_{0.4})_{1.01}CoO_{3-\delta}$
LSCO	$(La_{1-x}Sr_x)_yCoO_3$
LSCF	$La_{0.6}Sr_{0.4}Co_{0.2}Fe_{0.8}O_{3-\delta}$
LSCFO	$(La_{1-x}Sr_x)_yCo_{1-z}Fe_zO_3$
LSMO	$La_{1-x}Sr_xMnO_{3-\delta}$
LSCT	$(La_{0.6}Sr_{0.4})_{0.99}Co_{1-z}Ti_zO_{3-\delta}$
LSCT2	$(La_{0.6}Sr_{0.4})_{0.99}Co_{0.98}Ti_{0.02}O_{3-\delta}$
LSCT4	$(La_{0.6}Sr_{0.4})_{0.99}Co_{0.96}Ti_{0.04}O_{3-\delta}$
LSCT6	$(La_{0.6}Sr_{0.4})_{0.99}Co_{0.94}Ti_{0.06}O_{3-\delta}$
LSCT8	$(La_{0.6}Sr_{0.4})_{0.99}Co_{0.92}Ti_{0.08}O_{3-\delta}$
LSCT10	$(La_{0.6}Sr_{0.4})_{0.99}Co_{0.90}Ti_{0.10}O_{3-\delta}$
MIEC	mixed ionic and electronic conductor

n	an integral number
OCV	open-circuit voltage
OOR	oxide ion oxidation reaction
ORR	oxygen reduction reaction
p_{O2}	oxygen partial pressure
R	resistance
RC circuit	ohmic resistor in parallel with capacitor
RE	reference electrode
R_p	polarization resistance
R_s	high-frequency series resistance
RT	room temperature
SDC	$Sm_{0.15}Ce_{0.8}5O_{1.95}$
SEM	scanning electron microscope
SOC	solid oxide cell
SOEC	solid oxide electrolysis cell
SOFC	solid oxide fuel cell
T	temperature
TGA	thermogravimetric analysis
TOF-SIMS	time-of-flight secondary ion mass spectrometry
TPB	three-phase boundary
TEC	thermal expansion coefficient
U_0	steady-state potential
$U(t)$	alternating potential function on time
WE	working electrode
XPS	X-ray photoelectron spectroscopy
XRD	X-ray diffraction
W_s	Warburg diffusion impedance
YSZ	Y_2O_3–ZrO_2
Z_C	the impedance of the capacitor
Z_{RC}	the impedance of the RC circuit
$Z(t)$	impedance as the function of time
Z'	the real part of the impedance
Z''	the imaginary part of the impedance
α	a crystallographic angle
β	an integral breadth of the diffraction peak
θ	Bragg angle, the angle of diffraction
τ_k	time constant of individual RC circuit
φ	phase-shift
ω	angular frequency

3. INTRODUCTION

Fuel cells (FC) are unique systems for generating electricity from various fuels (H_2, CO, CH_4, etc.). FC produces electricity and heat from a gaseous fuel by electrochemical oxidation of the fuel with an oxidant. These devices achieve theoretical efficiency significantly higher than that of other conventional methods of power generation [1,2]. FC technologies are promising environmentally friendly devices for sustainable energy conversation. Energy demand is increasing rapidly, therefore the need for renewable energy resources is enormous [3]. Solid oxide fuel cells (SOFC) and solid oxide electrolysis cells (SOEC) work at high temperatures. SOFC is a device for fuel oxidation, and SOEC is for fuel production from excess electricity and steam or carbon dioxide. These technologies' advantages come from their high efficiency (electrical up to 60%, overall up to 85%). In addition, these systems offer high fuel flexibility [2]. Unfortunately, the wider use of these technologies is hindered by the high production costs of materials and the limited long-term stability of the materials during operation [2,4,5].

Perovskite-type (ABO_3) structure, mixed ionic and electronic conducting (MIEC) oxides are commonly used as SOFC oxygen electrode materials because of their high stability and moderate stability for temperature-caused segregation. [6]. Popular perovskite-type oxygen electrode materials are $(La_{1-x}Sr_x)_yCoO_3$ (LSCO) and $(La_{1-x}Sr_x)_yCo_{1-z}Fe_zO_3$ (LSCFO), both of which are excellent electrodes for oxygen reduction reaction (ORR) and oxide ion oxidation reaction (OOR) [7].

However, there are several throwbacks with LSCO-based oxygen electrodes. Under actual operating conditions and for simplicity of the system, it is necessary to use the air from the ambient atmosphere. Unfortunately, air from the ambient atmosphere contains different impurities, such as CO_2, H_2O, etc. [8,9]. LSCO-based materials have insufficient durability when these contaminants are present in the gas compartment. LSCO-based oxygen electrode materials have properties that will lead to cation rearrangement. In turn, this leads to the segregation of Sr to the surface, where it is accessible for contaminants, inducing the formation of unwanted phases ($SrCO_3$, $Sr(OH)_2$) [10]. $SrCO_3$ and $Sr(OH)_2$ are electrical insulators, therefore reducing electrode material activity for ORR. As a result, unwanted isolating phases form on the surfaces, blocking the active centers, changing the chemical composition on the perovskite surface compared with the composition in the bulk phase [11–13].

One way to improve stability of such materials is by modifying the perovskite structure with different valence elements at A- or B-sites. For example, introducing less active cation into the B-site decreases the Sr enrichment on the surface [14]. Overall, doping oxygen electrode material in B-site with higher valence cations improves the modified material against Sr segregation and therefore improve the overall material stability [15–18].

This work aimed to understand the influence of realistic working conditions, temperature, oxygen partial pressure, and electrode potential on the chemical composition and crystallographic parameters of several different electrode material groups, based on $(La_{1-x}Sr_x)_yCoO_3$ and $(La_{1-x}Sr_x)_yCo_{1-z}Fe_zO_3$. In addition, the influence of various contaminants (CO_2, H_2O) on the different oxygen electrode materials was studied. The main goal of the research was a systematic analysis of the influence of doping of $(La_{0.6}Sr_{0.4})_{0.99}CoO_{3-\delta}$ B-site with the higher valence Ti^{4+} cation.

4. LITERATURE OVERVIEW

4.1 Solid oxide cells

Solid oxide cells (SOC) are high-temperature devices that convert chemical energy into electricity via oxidizing fuels or produce sustainable green fuels by electrolysis of various chemical species, like H_2O.

SOC single cell consists of two porous electrodes (so-called oxygen and fuel electrode) with dense electrolyte layer in between (Figure 1). All those components need to fulfill a set of requirements. First of all, parts have to be mechanically compatible with each other. Oxygen electrodes need high electronic and ionic conductivities, optimized porosity, and high catalytic activity for oxygen reduction reaction (ORR). Fuel electrodes, however, need to combine catalytic activity for fuel oxidation, high ionic and electronic conductivities, as well as optimal porosity for fuel transport inside the electrode's microstructure. Compact electrolytes need high ionic conductivity but extremely low electronic conductivity at operating temperature. They also must be stable in both oxidizing and reducing atmospheres to avoid short-circuiting of electrodes [2].

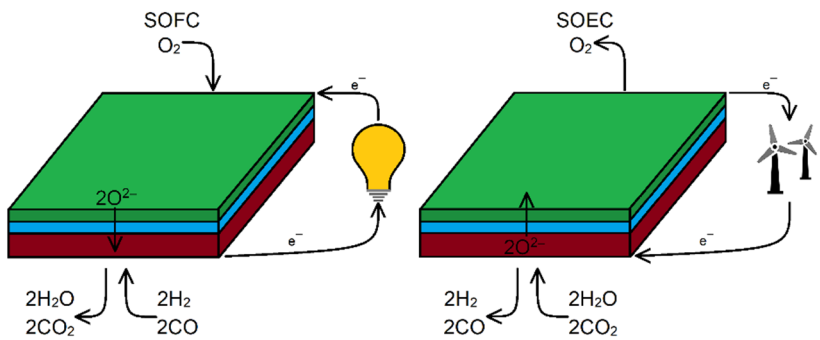

Figure 1. Illustration of the principle of SOCs in both solid oxide fuel cell (SOFC) and solid oxide electrolysis cell (SOEC) modes (noted in the figure). The upper green layer is a porous oxygen electrode, the middle blue layer presents a thin dense electrolyte, and the lower dark red layer is a porous fuel electrode.

If SOC operates in the fuel cell (FC) mode, the oxygen reduction occurs at the oxygen electrode (Eq. 1).

$$½O_2 + 2e^- \leftrightarrow O^{2-} \quad (1)$$

The oxide ion O^{2-} formed is conducted through the electrolyte to the fuel electrode. In the fuel electrode, the fuel oxidation (H_2, CO, etc.) occurs (Eq. 2).

$$H_2 + O^{2-} \leftrightarrow H_2O + 2e^- \quad (2)$$

There are different designs for SOCs. Due to all components being ceramic, SOC stacks can be configured into different shapes. The most common ones are planar and tubular designs. Planar design is more straightforward and cheaper to fabricate compared to tubular configuration. Tubular has its advantages. For example, gas-tight seals in a hot zone are unnecessary for a tubular design. On the other hand, tubular SOFC exhibit low current densities due to the long path of electrons to the current collector [1,19].

SOFCs are a revolutionary technology for environmentally favorable power generation, starting with the possibility to use different fuels because of the high operating temperatures from 600 °C up to 1000 °C [20]. Remarkable progress in materials and fabrication in the last decade has proved that even small systems (less than 300 kW) are capable of electrical efficiencies up to 60 % and overall efficiencies of 70–85 % [1,21].

4.2 Oxygen electrode materials for solid oxide fuel cells

The main function of the oxygen electrode is to provide active centers where the ORR occurs. The oxygen electrode material must be stable under an oxidizing environment and have mixed ionic and electronic conductivity (MIEC). It is crucial to have good conductivity to provide electron flow. Principally, the maximal oxygen electrode conductivity is essential to minimize the ohmic losses. Since the SOFC works at high temperatures (600 to 1000 °C), the oxygen electrode must be thermally and chemically compatible with other components of the FC within a very wide temperature region, i.e., from room temperature to the temperatures at which FC is fabricated. Thermal expansion coefficients (TEC) for different components must be close to each other to avoid cracking and delamination during fabrication and operation conditions. It is also vital for oxygen electrodes to have sufficient porosity to transfer the reacting gas to the reaction sites [1,2].

Because of the elevated working temperatures of SOFCs, the MIECs are suitable candidates for SOFC oxygen electrode materials. MIEC materials tend to have perovskite structures, which are usually nonstoichiometric oxides. Noble metals, stable at high temperatures, are not ideal for practical applications because of their high cost. Different doped oxides are possible options, but only a limiting number of MIEC have proven to be compatible with other cell components and meet the demand of TEC [1,2].

4.2.1 Perovskite-type electrode materials

Perovskite-type ABO_3 complex metal oxides can be used as catalysts. These complex oxides have a large variety of different applications (electrical, opto-, piezo-, magnetic materials). The perovskite lattice consists of oxide ions, large cations (usually rare-earth) in the A-site, and small transition metal cations in the

B-site. A-site cations are surrounded by 12 oxide ions. Therefore the B-site cations are surrounded by 6 oxide ions [1,2].

$La_{1-x}Sr_xMnO_{3-\delta}$ (LSMO) has been extensively used as SOFC oxygen electrode material because of its high electronic conductivity, about 200–300 S cm^{-1} at 900 °C [22,23], high electrochemical activity towards ORR at high temperatures, and high chemical stability with Y_2O_3–ZrO_2 (YSZ) electrolyte [1]. However, this material's oxygen ion conductivity is very low at < 700 °C [24], which prevents the use of LSMO as a SOFC oxygen electrode material at low temperatures as the ORR can only occur near the three-phase boundary (TPB) region (three phases: electrolyte, electrode, gas phase). Problems can also arise during the fabrication of cells. LSMO and YSZ react above 1200 °C and form unwanted $La_2Zr_2O_7$. Other reaction products can form during fabrication at high temperatures, including $SrZrO_3$ and different zirconate phases. The formation of insulating phases at the LSMO-YSZ interface induce the cell's degradation and create mechanical stress at the LSMO-YSZ interface. For example, $La_2Zr_2O_7$ and $SrZrO_3$ have several times lower electronic conductivity, and their TECs are also different from the main SOFC components [1]. Mixed YSZ/LSMO composites have been investigated intensively to improve the oxygen electrode material activity [25].

Doped $LaCoO_3$ is another perovskite-type oxide proven as a potential oxygen electrode material. $La_{1-x}Sr_xCoO_{3-\delta}$ shows enhanced electrocatalytic activity for ORR. It is also a better electronic and ionic conductor than LSMO at 600 to 800 °C. $La_{1-x}Sr_xCoO_{3-\delta}$ electronic conductivity at 800 °C can reach 1600 S cm^{-1} [26]. The great advantage of LSCO over LSMO is the ionic conductivity. At 800 °C $La_{0.6}Sr_{0.4}CoO_{3-\delta}$ ionic conductivity is 0.22 S cm^{-1} [27] compared to 1.7×10^{-4} S cm^{-1} of $La_{0.65}Sr_{0.35}MnO_{3-\delta}$ [27,28]. However, TECs of LSCO-based materials can be a drawback. Typically used electrolyte materials, like $Zr_{0.85}Y_{0.15}O_{1.92}$ or $Ce_{0.8}Gd_{0.2}O_{1.9}$ have the TECs 10.9×10^{-6} cm K^{-1} [29] and 12.7×10^{-6} cm K^{-1} [29] respectively, which is 2 times lower than $La_{1-x}Sr_xCoO_{3-\delta}$ (20.5×10^{-6} cm K^{-1}) [27]. Oxygen electrode materials used in SOFC must have similar TECs to other FC components. Mismatch of the TECs of the cell components will bring early cell failure due to mechanical stresses. The substitution of Fe^{3+} ions into the B-site of LSCO reduces the TEC values, but the catalytic activity for ORR also decreases. For example, $La_{0.6}Sr_{0.4}Fe_{0.8}Co_{0.2}O_{3-\delta}$ TEC is 17.5×10^{-6} cm K^{-1} [27] and $La_{0.8}Sr_{0.2}Fe_{0.8}Co_{0.2}O_{3-\delta}$ TEC is 14.8×10^{-6} cm K^{-1} [26]. Corresponding electronic conductivities are 302 S cm^{-1} [27] and 87 S cm^{-1} [27], respectively, and ionic conductivities 8×10^{-3} S cm^{-1} [27] and 2.3×10^{-3} S cm^{-1} [27].

It has been shown that introducing A-site deficiency can also somewhat improve the material's stability, catalytic activity, and conductivity. Creating A-site deficiency regulates oxygen vacancy formation and electronic structure, changing perovskite oxide-based material's properties. The oxygen vacancy formation is related to the electronic structure and the valence state of the transition metal [30–32]. For example, $LaFeO_3$ perovskite material's ORR kinetics can be enhanced by easily introducing A-site deficiency into the material.

It was shown that $La_{0.95}FeO_{3-\delta}$ was more active than the initial unmodified material. The increase in activity has been described by the formation of the oxygen vacancies and the formation of Fe^{4+} cations [32]. The positive effect of A-site deficiency on perovskite oxide materials stability is expressed in several ways. For example, it suppresses A-site component segregation and improves the exsolution of B-site cations. For instance, it was recently demonstrated that A-site deficient $Sr_{0.95}Nb_{0.10}Co_{0.90}O_{3-\delta}$ was more durable against CO_2 than $SrNb_{0.1}Co_{0.90}O_{3-\delta}$ [33].

Doping of the $LaCoO_3$ A-site with strontium can lead to new challenges. It has been shown that during fabrication and operating Sr^{2+} cation tends to segregate to the surface of the oxygen electrode. Sr segregation is considered one of the main reasons behind unstable perovskite oxide surfaces. When Sr segregates to the surface, it is more available for contaminants, which will induce the formation of secondary phases ($Sr(OH)_2$, $SrCO_3$). It has been shown that the existence of CO_2 and the formation of $SrCO_3$ accelerates the Sr segregation process and CO_2 oxidation [34]. The amount of Sr precipitated on the surface is influenced by oxygen partial pressure and temperature. An increase in temperature (up to 800 °C) increases the Sr segregation, while a decrease in oxygen partial pressure suppresses the Sr ions segregation [35]. Sr rich SrO and $SrCO_3$ are electrical insulators. They will lower the surface electrocatalytic activity of ORR and decrease the electrode electrochemical performance [36–38]. It has been shown that modification of materials with different valence elements at A- or B-site can improve material stability against Sr segregation. For example, doping B-site of $La_{0.8}Sr_{0.2}CoO_{3-\delta}$ with less-active (i.e., more stable oxidation state) cations like Al^{3+}, Ti^{4+}, Nb^{5+}, Zr^{4+}, Hf^{4+}, decreases the oxygen vacancy concentration at the electrode surface and therefore reduces the Sr surface compounds deposition on the surface [39]. It has also been demonstrated, that Fe cation has a positive effect on the stability of perovskite-type oxygen electrode material. For example, $La_{0.8}Sr_{0.2}Co_{0.8}Fe_{0.2}O_{3-\delta}$ has shown much higher thermal stability compared to $La_{0.8}Sr_{0.2}CoO_{3-\delta}$ in terms of electrochemical properties [40]. Overall, doping B-site of the oxygen electrode material with higher valence cations would improve the material stability against Sr segregation and therefore improve overall the material stability [16,18,41,42].

4.2.2 Perovskites electronic and ionic conductivity

All perovskite materials have similar electron conduction mechanism. ABO_3 structure builds up from the BO_6 network, and electronic conduction proceeds via holes or electrons on B-O-B links. The electronic conductivity of the oxygen electrode is determined by the electronic energies of the B-site cation since the energies of the cation 3d-orbital and the oxide ion 2p-orbital have to overlap partially. This interaction between cation d-orbital and oxygen ion 2p-orbitals causes the exchange of electrons or holes. Therefore, perovskite materials

containing transition metals with unfilled d-orbitals will have a great electronic conduction [28,43].

Moreover, following the above double exchange mechanism, achieving high electronic conductivity requires a B-site cation with multiple valences [28,44]. The electronic conduction can be n-type or p-type, depending on the material chemical and electrical characteristics. At high temperatures in an oxidizing environment, n-type electronic conductors are usually not stable since oxygen deficiency is needed to generate electrons. Inversely, p-type electronic conductors are commonly stable in the oxidizing environment or air because oxygen surplus is required to create holes [45]. Thus, the most suitable candidates for the B-site substitution are Cr, Mn, Fe, Co, and Ni cations. Oxide materials containing these cations provide high electrical conductivity.

Perovskite structure can have oxygen vacancies which are very important for the good oxide ion conductivity. The heterovalent substitution of cations with lower valence cations in the A- or B-site makes it possible to create vacancies in the perovskite structure. If perovskites already contain transition metal cations, then the formation of oxygen vacancies depends on the B-site cation's ability to change its oxidation state; therefore, the heterovalent substitution of cations does not always help form oxygen vacancies [28].

The oxide ion conductivity in perovskites are induced via a vacancy mechanism. Oxygen ions diffuse from occupied positions to vacant positions along the edge of a BO_6 octahedron. When an oxygen ion moves to the vacant position, it moves through the „gate“ formed by two A-site cations and by one B-site cation. The radius of this „gate“ formed by cations in perovskite should be similar to the oxygen ionic radius, which is 1.40 Å [28,46].

4.2.3 Mechanism of oxygen reduction on the oxygen electrode

The ORR takes place on the surface of a complex oxide material as a multistep mechanism. Also, this process can happen in several routes depending on the oxygen electrode material chemical composition, crystal structure, and on the nature of charge carriers in the electrode material [28].

The overall process starts with the reduction of oxygen molecules at the surface of the oxide, followed by the incorporation of O^{2-} ions into the lattice vacancies, which can be described with Kröger-Vink notations (Eq. 3)

$$^1/_2\, O_2\,(g) + V_{\ddot{O}} \rightarrow O_O^x + 2h^{\cdot} \tag{3}$$

The following possible steps of this complex process are:
adsorption of oxygen molecules on the surface of an oxide material or the electrolyte (Eq. 4),

$$^1/_2\, O_2\,(g) \rightarrow {}^1/_2\, O_2\,(ad) \tag{4}$$

dissociation of the molecules adsorbed (Eq. 5),

$$^1/_2\, O_2\,(ad) \rightarrow O(ad) \tag{5}$$

After the reduction of oxygen molecules to oxide ions they incorporate with vacant sites in the oxygen electrode lattice (Eq. 6)

$$O(ad) + 2e^- + V_{\ddot{O}} \rightarrow O_O^x \tag{6}$$

This process takes place in two parts, meaning that 2 electrons do not join simultaneously. The first electron affinity of oxygen is -141 kJ mol^{-1} [47], and the second electron affinity of oxygen is 744 kJ mol^{-1} [48]. Also, the last step can occur either on the TPB or on the oxygen electrode material, depending on the nature of the electrode material. If the material has excellent electronic and ionic conductivity, the last step occurs on the surface of the electrode. If ORR happens on the electrode surface, then the oxide ions formed from oxygen are incorporated into the electrode material, and then they are carried in the solid phase to the electrode/electrolyte interface [28].

The ORR rate is lower for oxygen electrode materials with reduced oxide-ion conductivity, and the material characteristics (corresponding resistance and activation polarization characteristics, etc.) depend on the TPB's length. Thus, it is crucial to decrease the particle size to reach moderate activity and lower resistance values. Still, it is not easy to prepare the high TPB materials working at high temperatures because the average size of particles increases with increasing temperature and working time applied [2].

4.3 Electrochemical impedance spectroscopy

Electrochemical impedance spectroscopy (EIS) is a powerful and non-destructive method for characterization of the electrical properties of different materials and their interfaces. This method can be applied for the investigation of the dynamics of bound or mobile charge carriers in the bulk or interfacial regions of any solid or liquid materials characteristics [49].

EIS experiment involves excitation of the system under study with steady-state potential and low-amplitude alternating (AC) potential and measuring the current response. Voltage perturbation signal can be expressed as:

$$U(t) = U_0 \sin(\omega t) \tag{7}$$

where $U(t)$ is an alternating potential function on time, U_0 is steady-state potential, $\omega = 2\pi f$, where f is the frequency. The current response to the voltage perturbation is then expressed as:

$$I(t) = I_0 \sin(\omega t - \varphi) \tag{8}$$

where $I(t)$ is the alternating current function on time, I_0 is the maximum amplitude of the current, and φ is the phase shift between the voltage and current waveforms.

The relationship between applied alternating potential and the resulting alternating current is impedance and can be expressed as:

$$Z(t) = \frac{U(t)}{I(t)} \tag{9}$$

where $Z(t)$ is the impedance as the function of time, impedance has both magnitude and a phase-shift φ, making it a vector quantity. Usually, impedance is measured for a large set of frequencies and can be expressed by a complex number of the vector sum of real (Z') and imaginary (Z'') parts:

$$Z(\omega) = Z'(\omega) + iZ''(\omega) \tag{10}$$

where $i = \sqrt{-1}$. A Nyquist plot is obtained when plotting the real part against the imaginary part (Figure 2).

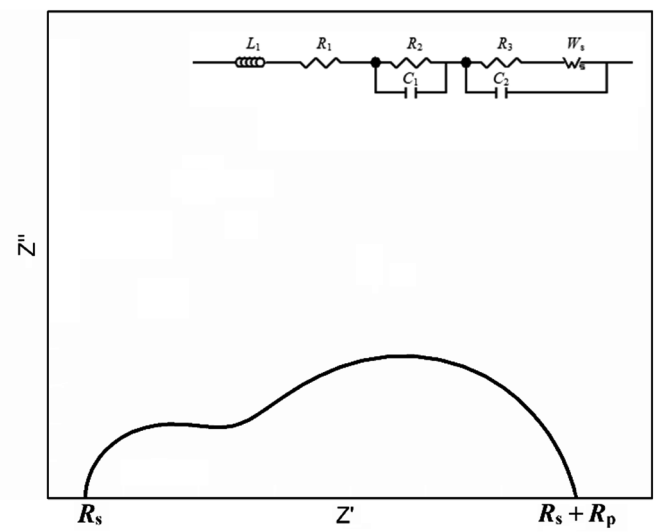

Figure 2. Experimental Nyquist plot with corresponding equivalent circuit.

The first intercept at relatively high frequencies in the SOFC Nyquist plot usually correlates to the high-frequency series resistance or ohmic resistance, R_s, of the system. The resistance of the dense electrolyte mainly causes an R_s value. The resistance between high and low-frequency intercepts of the real axis corresponds

to the polarization resistance, R_p, of the system under study. R_p combines all reaction resistances in both electrodes, including charge transfer, mass transfer steps, and adsorption limitations steps resistances. Depending on the values of time constants of different processes occurring in the studied systems, the Nyquist plot may have a complicated shape and contain one or multiple semi-circles and even nearly linear areas [2,50].

Single SOFC electrodes can be characterized in symmetrical cells with identical electrodes (2-electrode setup) at open-circuit voltage (OCV) conditions (0 V AC potential with small AC perturbation). Measuring in OCV conditions results in both electrodes and gives the sum of both electrode polarization resistances. If both electrodes are identical, the one electrode polarisation resistance is half of the total value. The downside of this method is that this measurement can not be conducted under *operando* conditions (no current passes within the cell). To characterize one electrode under operating conditions, a 3-electrode setup can be used. 3-electrode setup consists of a working electrode (WE), counter electrode (CE), and reference electrode (RE). The small AC potential is applied over specific DC potential in this method. This method's drawback is that this setup is not ideal for accurate impedance studies. Different errors can occur with the misplacement of electrodes. It has been shown that very small misplacement (by 0.2 mm) of WE and CE can cause a moderate error in R_p value [51]. With a 3-electrode design, it is extremely important to align electrodes precisely to minimize errors. Also, the distance between WE and RE should be at least two times or more than the electrolyte thickness [51–54].

4.3.1 Fitting of impedance spectra

Analyzing the data established by EIS, some conclusions about the processes occurring at electrodes are possible. EIS does not give information about the background of the physical processes, but comparing acquired data with physical models and model systems can help to understand the rate-limiting processes [55]. To improve the SOFC properties, it is essential to know the reasons behind the activity losses and possible degradation mechanisms. EIS differentiates various processes by their time constants. Different physical processes have different time constants for describing the dominating limitating processes during SOFC/SOEC operation. Usually, changes in the processes taking place in the system are evaluated with a pretty primitive approach using a series of semi-circles, forming equivalent circuit (EC) and linking them with probable specific processes. Such an analysis method is based on interfaces' physical processes and reaction steps discussed in the literature [49].

Thus, usually, a systematic analysis of Nyquist plots helps to describe processes taking place on the electrode. The high-frequency part (f > 20 kHz) describes the ohmic resistance region, where limiting processes are electrolyte bulk phase resistance and electrical contact wire resistance. Next region (20 kHz > f > 50 Hz) describes processes like bilayer loading and Faraday

processes on mesopores and finite-length interparticle interfaces. Low-frequency (f < 50Hz) part usually describes mass and charge transfer processes taking place in smaller meso- and micropores [56,57].

The impedance data measured in this study were modeled using EC given in Figure 3, where L_1 is the high-frequency inductance, R_1 is very high-frequency series resistance, R_2 is high and medium frequency charge transfer resistance, and R_3 is high low-frequency charge transfer resistance. C_1 and C_2 are capacitances, which are replaced with the *CPE* (constant phase element) in some cases (to compensate for the non-homogeneity in the system). W_s is the so-called Warburg diffusion element that models mass transfer resistance.

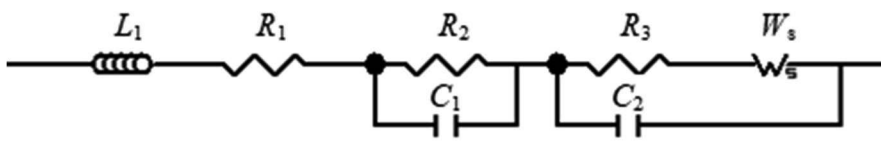

Figure 3. The equivalent circuit was used to fit experimental impedance data.

The distribution of relaxation times (DRT) analysis method was also used to distinguish the processes occurring on the electrode. DRT is a powerful tool that converts measured electrochemical impedance spectra from frequency into the time domain, taking the Fourier transform of the spectrum into the focus. DRT analysis allows more accurate information about how different processes contribute to total polarization resistance, R_p. The advantage of the DRT method over impedance spectroscopy is the ability to differentiate mathematically processes that might be overlapping in impedance spectroscopy [58].

The DRT analysis is based on the distribution of predefined relaxation times. The DRT method approximates the measured impedance data to a model consisting of RC elements (ohmic resistor in parallel with capacitor with impedance $Z_C = (j\omega C)^{-1}$)) with different time constants. Parallel RC circuit resistance is given by formula (11):

$$Z_{RC} = \frac{R}{1+\mathrm{j}\omega\tau_{RC}} \tag{11}$$

where τ_{RC} is the characteristic time constant. Usually, a series of RC circuits with individual time constants is τ_k used to describe how every RC circuit is contributing to the total polarization resistance ($h_1, h_2, \mathrm{h_k}$). The h_k value gives information about the resistance of the corresponding RC element. The DRT impedance spectrum can be described with the formula (12):

$$Z_{DRT} = R_p \times \sum_{k=1}^{N_\tau} \frac{g_k}{1+\omega\tau_k} = \sum_{k=1}^{N_\tau} \frac{h_k}{1+\omega\tau_k} \tag{12}$$

where g_{k} is the normalized distribution of relaxation times function. Parameter g_{τ} gives information about the relative contribution to the total polarization resistance, but h_{τ} gives some information about the total contribution of the single process [58–60].

4.4 X-ray diffraction

SOC electrodes and electrolytes are usually polycrystalline, and the properties of these materials are determined by the crystallographic properties and chemical composition of different phases expressed in the material under study. X-ray diffraction (XRD) makes it possible to analyze and assess the phase purity, determine the structure, and give information about crystallographic bulk properties.

Crystalline solids consist of regular arrays of atoms, ions, or molecules. Typically the interatomic spacing is in the order of 100 pm. For diffraction to occur, the wavelength of the incident light must be of the same order of magnitude as the distance of the gratings. The maxima in the diffractogram result from constructive interference between monochromatic X-ray waves that have elastically scattered from the different lattice planes. Bragg equation (13) relates the spacing between the crystal planes to the particular Bragg angle at which the reflection from these planes is observed.

$$n\lambda = 2d\ sin\theta \tag{13}$$

where n is an integral number, λ is the wavelength of the X-ray, d is the distance between lattice planes, and θ is the angle of diffraction (Bragg angle) [61].

As a result of systematic research, it was shown that the maximum width observed in the diffractogram depends on the size of the crystallite. The decrease in crystallite size results in an expansion of the diffraction peak. Theoretically, diffractive rays should provide non-constructive interference on both sides of the Bragg corner, and the diffraction maximum should be sharp. This is only the case for large regular crystallites, where the aggregation of diffracted rays over the whole sample takes place. The smaller the crystallites, the lower the atomic levels from which the condition of destructive interference would be fulfilled if diffracted even with a slight deviation from the Bragg angle. This leads to an expansion of the diffraction maximum.

Usually, the Debye-Scherrer formula (14) is used to find the crystallite size:

$$D = \frac{K\lambda}{\beta cos\theta} \tag{14}$$

where D is the mean or actual crystallite size, K is a dimensionless shape factor (Scherrer constant), λ is the X-ray wavelength, β is an integral breadth of diffraction peak (after subtracting the instrumental line broadening), and θ is the angle of diffraction (Bragg angle) [61].

5. EXPERIMENTAL

5.1 Preparation of single cells

Studied oxygen electrode powders with different compositions (Table I) were synthesized using the thermal treatment method, i.e., combustion of the corresponding nitrate and oxalate solutions, where $La(NO_3)_3 \cdot 6H_2O$, $Sr(NO_3)_2$ (both from Aldrich, 99.9%), $Co(NO_3)_2 \cdot 6H_2O$ (98%, Riedel de Haën), $Fe(NO_3)_3 \cdot 9H_2O$ (Merck, 99 %), $(NH_4)_2TiO(C_2O_4)_2 \cdot xH_2O$ (Puratronic, 99.998%) were used as precursors and glycine (99%, Sigma-Aldrich) as the reducing agent [62–64]. Viscous electrode pastes were made using polyethene glycol (Sigma-Aldrich) as a plasticizer, polyvinyl butyral (Sigma-Aldrich) as a binder, terpineol, and Solsperse 3000 (Lubrizol) as solvent components and dispersant, respectively.

Table I. Studied oxygen electrode materials and their abbreviations.

Oxygen electrode material	Abbreviation
$La_{0.6}Sr_{0.4}CoO_{3-\delta}$	LSC
$(La_{0.6}Sr_{0.4})_{0.99}CoO_{3-\delta}$	LSC99
$(La_{0.6}Sr_{0.4})_{1.01}CoO_{3-\delta}$	LSC101
$(La_{0.6}Sr_{0.4})_{0.99}Co_{0.98}Ti_{0.02}O_{3-\delta}$	LSCT2
$(La_{0.6}Sr_{0.4})_{0.99}Co_{0.96}Ti_{0.04}O_{3-\delta}$	LSCT4
$(La_{0.6}Sr_{0.4})_{0.99}Co_{0.94}Ti_{0.06}O_{3-\delta}$	LSCT6
$(La_{0.6}Sr_{0.4})_{0.99}Co_{0.92}Ti_{0.08}O_{3-\delta}$	LSCT8
$(La_{0.6}Sr_{0.4})_{0.99}Co_{0.90}Ti_{0.10}O_{3-\delta}$	LSCT10
$La_{0.6}Sr_{0.4}Co_{0.2}Fe_{0.8}O_{3-\delta}$	LSCF
$La_{0.6}Sr_{0.4}CoO_{3-\delta}$ + $La_{0.6}Sr_{0.4}Co_{0.2}Fe_{0.8}O_{3-\delta}$	LSC + LSCF

Symmetrical cells used in the studies were prepared using gadolinia-doped ceria ($Ce_{0.9}Gd_{0.1}O_{2-\delta}$) (GDC) electrolyte pellet as the support with a thickness d_{el} of nearly 750 μm [62–64]. For $(La_{0.6}Sr_{0.4})_{0.99}Co_{1-x}Ti_xO_{3-\delta}$ test series, symmetrical cells were prepared onto samaria-doped ceria (SDC) electrolytes. Raw paste of the electrolyte pellets were prepared using commercially available $Sm_{0.15}Ce_{0.8}5O_{1.95}$ powder (SDC-15, NexTech Materials), ethanol (Merck, 99.5%), xylenes (mixture, Honeywell, ⩾ 98.5%), menhaden fish oil (Sigma-Aldrich) as a dispersant, Butvar-B98 (Sigma-Aldrich) as the binder, benzyl butyl phthalate (Merck, 96%) and polyethene glycol (Sigma-Aldrich) as the plasticizers. Electrolyte membrane tapes were cast using AFA I Automatic Thick Film Coater (MTI Corporation) with a speed of 40 mm s^{-1}. Four tapes were isostatically laminated with sufficient thickness (isostatic laminating system ILS 46, Keko Equipment), followed by sintering at 1400 °C for 5 h. The thickness of the dense sintered electrolyte was about 240 μm.

The micro-mesoporous electrodes with a geometrical flat-cross section surface area of 1.77 cm^2 (both working and counter electrode) were screen printed onto the GDC electrolyte (article I–III). The porous electrodes with a geometrical flat-cross section surface area of 0.38 cm^2 were screen printed onto the SDC electrolyte (article IV). The symmetrical electrodes deposited onto GDC and SDC were sintered at 1100 °C for 5 hours [62–64]. Electrical contacts were taken using porous platinum contact layers formed from Pt paste (MaTeck) after heating at T = 950 °C, connecting Pt contacts through the platinum fires to the Solatron measurement system.

5.2 Physical characterization methods

XRD analysis of the synthesized powders and prepared electrode materials was carried out using Bruker D8 Advanced Diffractometer with Cu Kα_1 radiation (λ=1.540596 Å) source (40 kV, 40 mA), Vario1 focusing primary monochromator, two 2.5° Soller slits, and a LynxEye 1D detector.

X-ray thermo-diffractometry study has been performed in an Anton Paar HTK 1200 N temperature vessel. The sample was placed in an alumina sample holder and heated in different oxygen concentrations from room temperature (RT) up to 800 °C. For XRD studies 60-minute continuous scan from 21 to 75° 2 θ with 0.015° 2 θ step, and with a total count time of 166 seconds per step, was applied. A single peak scan experiment was performed from 57.5 to 59.5° with 0.015° 2 θ step and 40 seconds total count time per cycle.

Completed porous oxygen electrodes and single cells were characterized using Zeiss EVO® MA 15 scanning electron microscope (SEM). For more detailed information, Helios™ NanoLab 600 (FEI) high-resolution SEM was used.

The microstructural and chemical changes for studied oxygen electrode materials during different operando working conditions were visualized using time-of-flight secondary ion mass spectrometry (TOF-SIMS) (PHI TRIFT V nanoTOF instrument).

Thermogravimetric analysis (TGA) was performed using the Netzsch STA 449 F3 Jupiter thermal analyzer for all synthesized powders within the temperature range from 30 °C to 1100 °C with a heating and cooling rate of 5 °C min^{-1} and a gas flow rate of 80 ml min^{-1}. The analysis was conducted in synthetic air (pO_2 = 0.2 atm, pN_2 = 0.8 atm) and in an N_2 (purity 99.999 %) environment.

X-ray photoelectron spectroscopy (XPS) measurement for different oxygen electrode materials working in different conditions was measured by the hemispherical analyzer (Scienta SES100) at a pass energy of 200 eV and using Al-Kα radiation with an overall resolution of approximately 0.8 eV.

5.3 Electrochemical characterization

During electrochemical measurements the working electrode potential was controlled using Solartron 1470E potentiostat and Solartron 1455 A frequency response analyzer, and Solatron 1287A potentiostat/galvanostat completed with the electrochemical interface. In addition with XRD measurements, the impedance spectra were measured using Solartron 1260 frequency response analyzer. The impedance spectra were measured in a three-electrode setup (from 1 MHz to 0.01 Hz) with the ac amplitude 15 mV. Electrochemical data were analyzed using Zview and Corrview software (Scribner Associates Inc.). The single cells were electrochemically characterized at gas overflow conditions, where the gas flows were controlled by EL-FLOW SELECT F210CV mass-flow controllers (Bronkhorst). The symmetric cells were investigated at different temperatures from 500 – 800 °C and with different gas compositions: at different oxygen contents (3%, 10%, 20%, 50%), in synthetic air (21% O_2 and 79% N_2), in synthetic air with addition of 10% CO_2 (21% O_2 and 69% N_2, 10% CO_2), and in synthetic air (21% O_2 and 79% N_2) with 1.7 % and 3% H_2O addition, respectively.

6. RESULTS AND DISCUSSION

6.1 Physical characterization of oxygen electrode materials

6.1.1 X-ray diffraction data for synthesized materials

The characteristic XRD patterns for LSC, LSCF, and LSC + LSCF mixed electrodes measured at T = 600 °C are given in Figure 4, where the different materials and crystallographic orientations have been noted. The XRD maxima for LSC and LSCF materials are pretty narrow and well expressed, referring to the excellent crystallinity of LSC and LSCF (Figure 4). Somewhat broader peaks can be seen for LSC+ LSCF (50:50 wt%) oxygen electrode. As the oxygen electrodes are only about 20 μm thick, the weak GDC electrolyte reflections can be seen in some diffractograms for samples. Small Au clusters, giving XRD maxima in Figure 4, were deposited for calibration purposes. No unwanted phases like carbonates (synthesis products in raw powder) or $CoFe_2O_4$ (which can be formed under electrical polarization conditions) have not been found based on XRD data. However, perovskite phase with comparable crystallographic parameters have been detected [65,66]. The parameters calculated are given in Table II. The rhombohedral phase *R3c*, is characterized by lattice constant a and a crystallographic angle α, given in Table II.

The XRD data of $(La_{0.6}Sr_{0.4})_{0.99}Co_{1-z}Ti_zO_{3-\delta}$ (LSCT) oxygen electrode material powders measured at room temperature (RT) are shown in Figure 5. The diffraction maxima for the LSCT oxygen electrode materials characterized in this work refer to a perovskite structure with a space group of *R3c* and an SG number of 167 [67]. Reflections from other unwanted phases cannot be found in the XRD patterns. As demonstrated in Figure 5, doping B-site of LSC99 with bigger cation commences the shift of maximum to lower 2θ values, indicating that the lattice parameters and unit cell volume increase with increasing Ti content in the B-site compared to non-substituted material (Table II). This is caused by the larger ionic radius of Ti^{4+} (0.61 Å) compared to Co^{4+} (0.53 Å) ions. Also, cation with higher valence (Ti^{4+}) probably affects the oxidation state of the B-site cation (reduction of Co^{4+} to Co^{3+} (0.61 Å)), which leads to the expansion of $La_{0.6}Sr_{0.4}CoO_{3-\delta}$ lattice [68]. It can also be seen that a more intensive change in the lattice takes place for materials with 8% and 10% of Ti cations in the B-site. It has been shown that increasing the B-site cation radius makes the lattice more hexagonal [69].

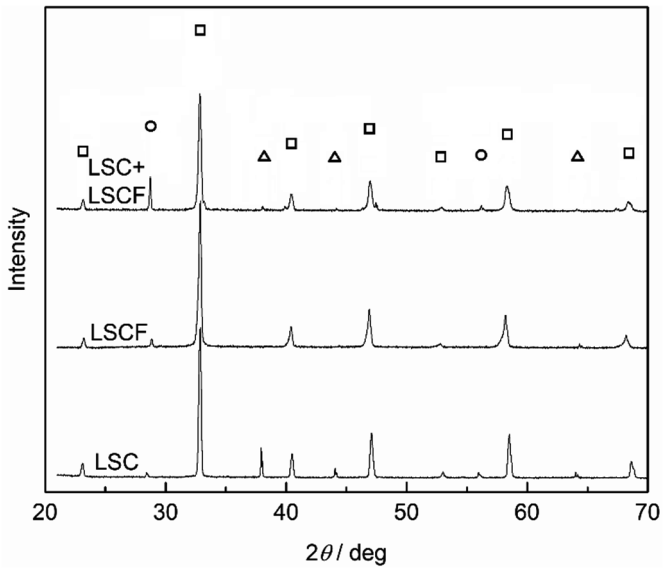

Figure 4. XRD patterns for studied LSC, LSCF, and LSC + LSCF (50:50 wt%) oxygen electrodes at working temperature $T = 600$ °C, oxygen partial pressure $p_{O2} = 0.2$ atm, and at oxygen electrode potential $E = 0$ V. The phase of the perovskite is indicated by a square, phase of GDC is indicated by circle and phase of Au is indicated by a triangle, noted in the figure.

Table II. Lattice parameters for studied oxygen electrode powders and oxygen electrodes. Electrodes (with *R3c*) were characterized at 600 °C and with oxygen partial pressure $p_{O2} = 0.2$ atm.

Material	a (Å)	c (Å)	α (°)
LSC99 powder, RT	5.4324	13.2366	-
LSCT2 powder, RT	5.4348	13.2349	-
LSCT4 powder, RT	5.4362	13.2389	-
LSCT6 powder, RT	5.4385	13.2434	-
LSCT8 powder, RT	5.4399	13.2546	-
LSCT10 powder, RT	5.4399	13.2569	-
LSC electrode, $T = 600$ °C	5.4726	-	59.9641
LSCF electrode, $T = 600$ °C	5.5119	-	60.1502
LSC + LSCF electrode (for LSC), $T = 600$ °C	5.4907	-	59.9102
LSC + LSCF electrode (for LSCF), $T = 600$ °C	5.4969	-	60.0777

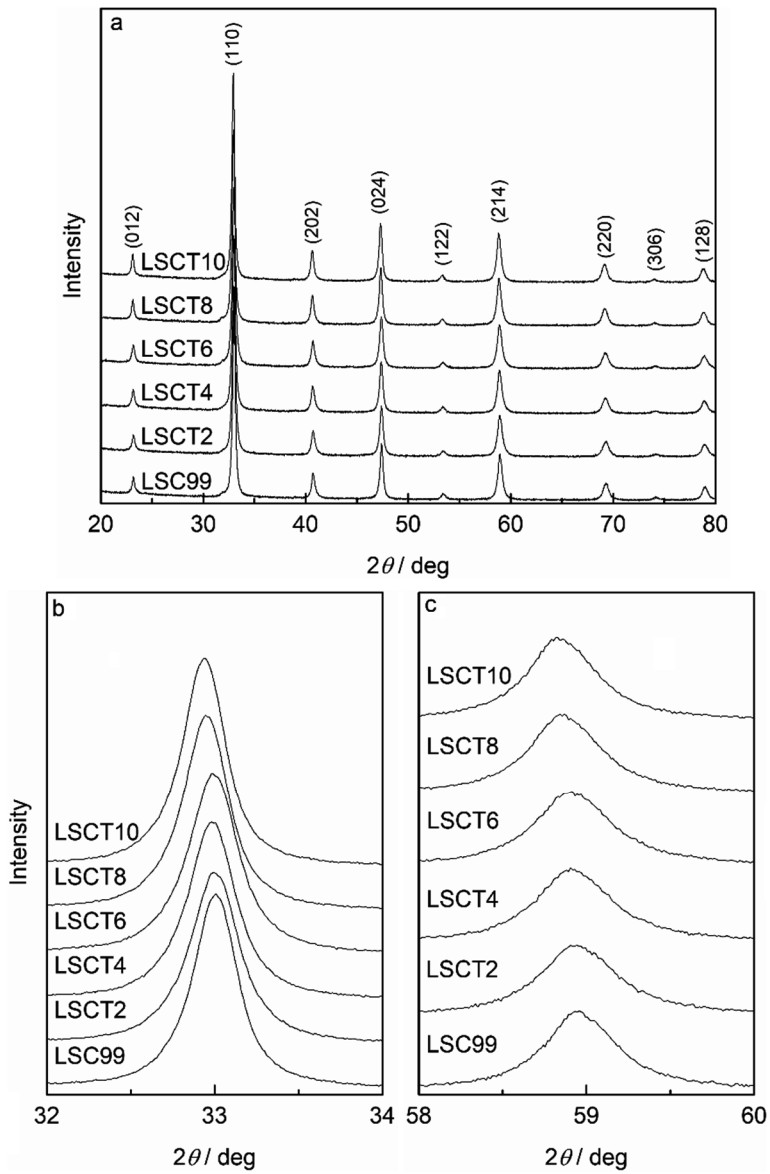

Figure 5. XRD patterns for studied oxygen electrode powders (a). The meaning of acronyms used in the figure are described in Table I. Shift of (110) (b) and (214) (c) reflection as a function of Ti concentration in the B-site of LSCT.

6.1.2 Influence of temperature, oxygen partial pressure, and oxygen electrode negative potential on the lattice parameters

Data in Figure 6 shows the influence of the oxygen partial pressure, temperature, and oxygen electrode negative potential on the crystallographic unit cell parameters measured for LSC oxygen electrode material. LSCF has a bigger unit cell volume than LSC (Figure 7), which is in agreement with the literature data [70], showing that iron ions substituted into B-site expands the crystal lattice. Increasing oxygen partial pressure by 0.1 atm increases the unit cell volume by about 0.004 $Å^3$. The results are consistent with the notion that the lattice volume or vacancy concentration increases with the decrease of the oxygen partial pressure in the electrode compartment. D-metals can change the oxidation state; therefore, the charge neutrality was achieved, and the cations having interactive influence caused the expansion of the lattice of oxygen electrodes under study.

Results in Figure 6 indicate that increasing oxygen electrode negative potential increases the cell volume, generating more vacancies. It can be seen that oxygen electrode negative potential has more influence on the lattice parameters at lower oxygen partial pressure. Almost linear increase of unit cell volume can be obtained at fixed oxygen partial pressure with the rise of oxygen electrode negative potential, which can be described with the Co^{4+} reduction to Co^{3+}. The volume change of LSC and LSCF unit cells are in the same order. Every –0.1 V applied potential increases the unit cell volume by nearly 0.08 $Å^3$, if $p_{O2} = 0.03$ atm. It can also be concluded that the polarized oxygen electrode crystallographic structure is more sensitive to the oxygen partial pressure changes. It can be described as the decrease of the effective oxidation state of cobalt ions. Therefore, the oxygen separation from the structure is achieved more easily. At lower $T \leq$ 500 °C, there is no clear dependence of the cell volume on the oxygen electrode potential applied as in this region of temperature, the phase transition from *R-3cH* unit cell to *R-3cR* takes place for studied electrodes [71].

At fixed temperature and 0 V, the influence of oxygen partial pressure on the cell volume is weak. Only a tiny decrease of volume with p_{O2} has been observed, indicating that the concentration of vacancies almost does not depend on the O_2 partial pressure in the gas phase. Still, at $E = –0.7$ V (vs. $Pt/Pt/O_2$), the influence of oxygen partial pressure is remarkable.

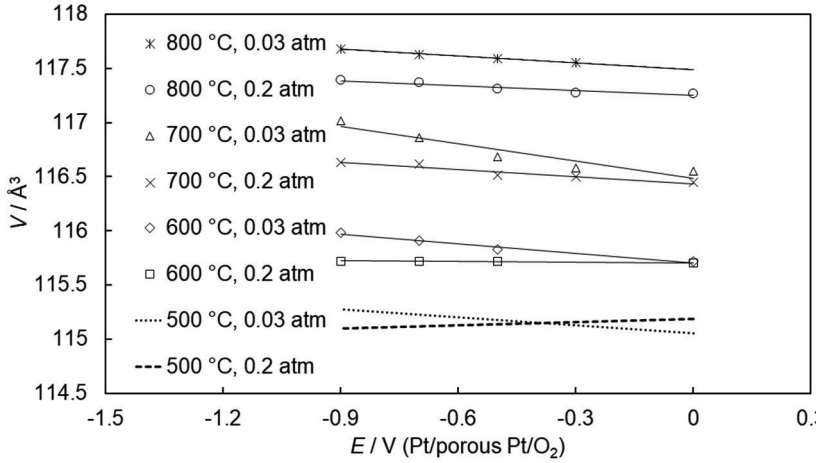

Figure 6. The cell volume vs. oxygen electrode potential plots for LSC at fixed O_2 partial pressure and at fixed working temperatures, noted in the figure.

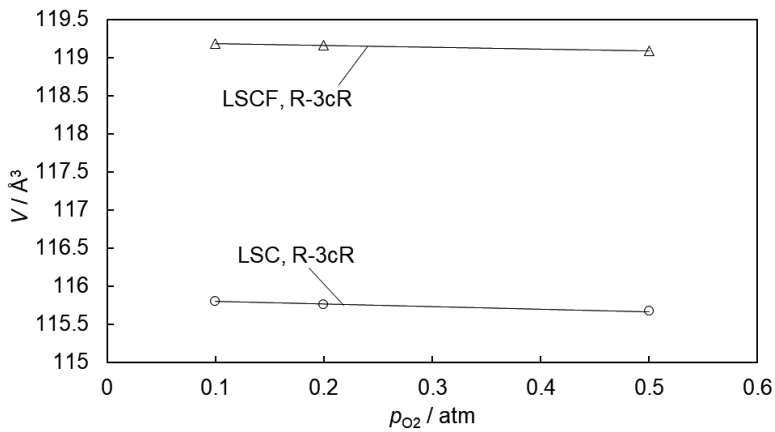

Figure 7. The cell volume vs. oxygen partial pressure plots for LSC and LSCF oxygen electrodes (noted in the figure) at a working temperature of 600 °C and at oxygen electrode potential E = 0 V (vs Pt/porous Pt/O_2).

6.1.3 Kinetic response of lattice parameters to oxygen electrode potential change

The influence of oxygen electrode negative potential on the position of one of the characteristic maximum is given in Figures 8 and 9. In general, it can be concluded that the maximum position shift is reversible. The initial diffractograms at 0 V were measured four times, and potential –0.9 V was applied. The measured maximum was higher, narrower than the initial maximum, and shifted

to lower 2θ values. As described earlier, the volume of crystallographic unit cells has expanded, and vacancy concentration has increased with applying a negative potential to the oxygen electrode. The increase in maximum height is due to ions achieving higher regularity in the crystal structure [72]. After 20 cycles at –0.9 V, the potential was changed back to 0 V, and the maximum shifted back to the initial 2θ values. The LSC unit cell volume increases nearly by 0.08 Å^3 for every 0.1 V increase of the cathodic polarization if p_{O2} = 0.03 atm.

At temperatures higher than 600 °C, the peak halfwidth value is unchanged since the potential step and the equilibrium state reaches faster than 40 sec, which is the time that takes to scan one smallest XRD segment (Figure 8). At lower oxygen partial pressures and temperatures, the peak position and halfwidth are more responsive for negative oxygen electrode potential than those observed at high temperature and oxygen partial pressure. The XRD maximum is higher and narrower in a negative electrode polarization condition than in the non-polarized state, which indicates that better crystallographic symmetry has been achieved under negative electrode potential.

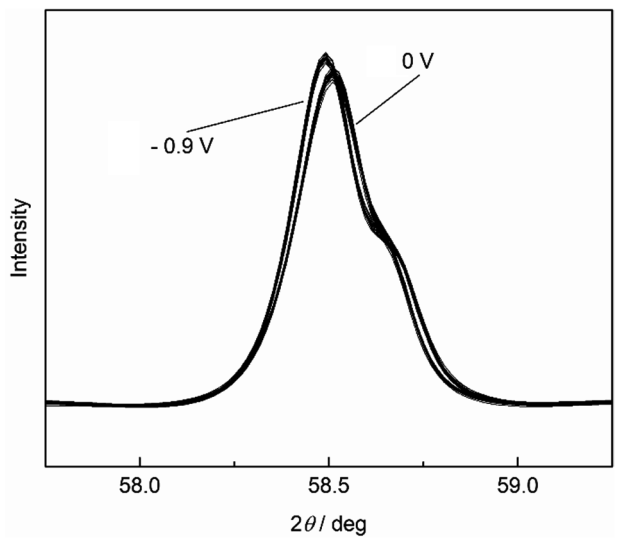

Figure 8. The segment from the XRD pattern ((214) with $K_{\alpha 2}$ reflection) for LSC oxygen electrode at electrode potentials 0 and –0.9 V vs Pt/Pt/O_2, respectively, and at T = 600 °C and p_{O2} = 0.2 atm. Segments were measured for every 40-second interval.

It can be concluded from Figure 9 that the effect of electrode potential on the XRD data is not immediate. At a lower temperature (500 °C), at least one intermediate maximum is present on the diffractogram segment, indicating the existence of the intermediate structure formation (no stabilized situation). Maximum shift to stabilized state takes longer than 40 seconds because one XRD

measurement cycle takes approximately 40 seconds. The maximum „X“ describes the intermediate maximum changing electrode potential from 0 V to –0.9 V and maximum „Y“ represents the intermediate maximum when electrode potential is changed from –0.9 V to 0 V. The kinetic behavior of the crystal lattice relaxation for the potential step from 0 V to −0.9 V and from −0.9 V to 0 V is different. This is probably due to the different kinetics of oxygen incorporation from the gas phase and the rate of release of oxygen from the lattice.

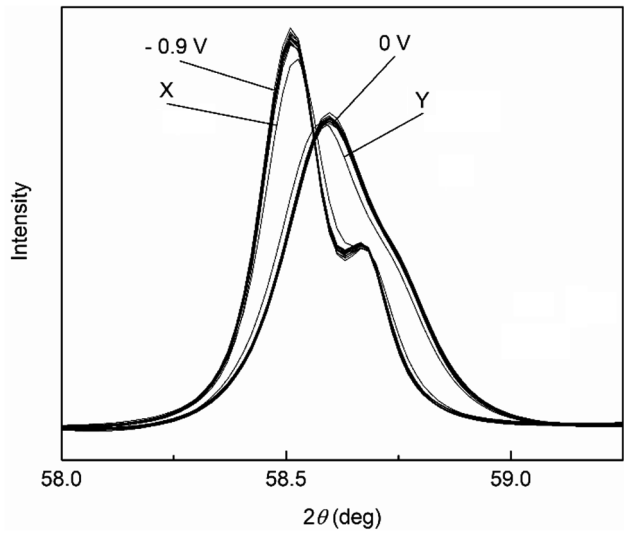

Figure 9. The Segment from the XRD pattern ((214) with $K_{\alpha 2}$ reflection) for LSC oxygen electrode at electrode potentials 0 and −0.9 V vs $Pt/Pt/O_2$, respectively, and at T = 500 °C and p_{O2} = 0.2 atm. Segments were measured for every 40-second interval.

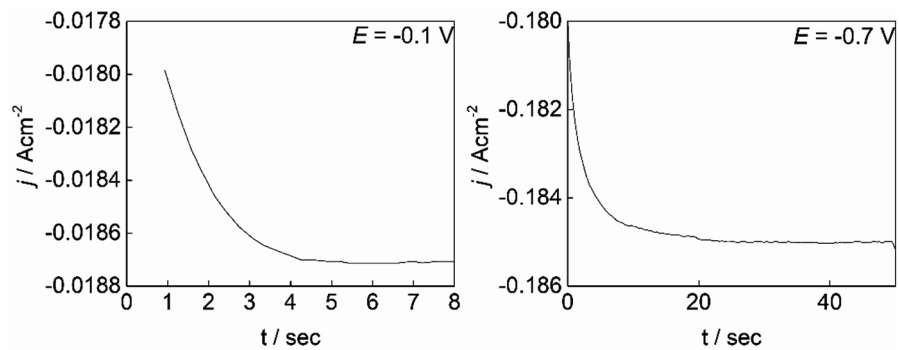

Figure 10. The LSC chronoamperometric plots at different negative electrode polarization (noted in the figure) at T = 600 °C and p_{O2} = 0.2 atm.

Impedance spectra measured in our work are unsuitable for analyzing kinetic impact with relaxation time longer than 40 sec. We used chronoamperometric curves in response to the potential step to track the stabilization time followed by the potential change (Figure 10). The stabilization times and the peak relaxation times in HT-XRD are similar. Stabilization times calculated from chrono-amperometry curves are systematically longer, but the more time-consuming final reorganization process could explain this at the interfacial layer. This does not influence the HT-XRD data much but has some influence on the electro-chemical parameters.

6.1.4 Thermogravimetric analysis of CO_2 treated oxygen electrode powders

The TGA results for the CO_2-treated LSC99 powder measured in a pure N_2 environment and synthetic air are given in Figure 11a. The weight decrease can be seen for both samples within the temperature range 30 °C to 1100 °C. The sample measured in an N_2 environment resulted in a more extensive mass change. This mass change is due to the oxygen vacancy formation and oxygen desorption from the oxygen electrode surface [73]. In synthetic air, mass change is not so significant. The oxygen chemical potentials in the bulk and gas phases are different, and therefore, the oxygen desorption is trivial from the oxygen-rich environment. As shown in Fig 11a, the mass of the sample at the beginning and the end of the thermal cycle is the same. Thus, we can conclude that no de-composition of carbonates took place during the thermal cycle. The mass loss at elevated temperatures is caused by the oxygen evolution released from the lattice. At higher oxygen concentrations, the vacancy concentration change is nearly reversible. In the case of low oxygen concentrations in the gas phase (LSC99 in N_2), the initial plateau is not achieved, and the oxygen partial pressure determines the vacancy concentration.

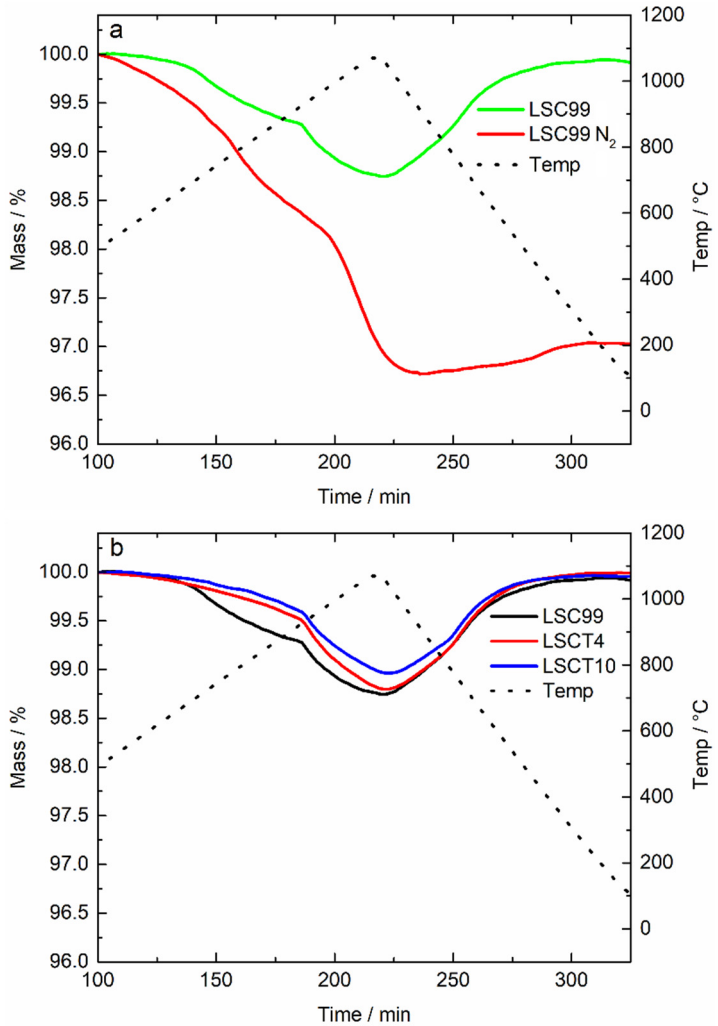

Figure 11. The TGA curves for the LSC99 were measured in pure N_2 and a synthetic air environment (a), and TGA curves for the LSC99 and LSCT4 and LSCT10 were measured in a synthetic air environment (b).

Doping the LSC99 oxygen electrode material with Ti cation improves the stability of the lattice (Figure 11b). For LSC99, the oxygen vacancy formation is more extensive than for LSCT, showing that modifying B-site with Ti cations controls the Co cation oxidation state and improves the stability of the material.

6.1.5 X-ray photoelectron spectroscopy analysis of the effect of CO_2 and H_2O on the oxygen electrode materials

The material's electronic structure defines the catalytic properties of the MIEC surface towards ORR. Therefore, XPS measurements were conducted to understand the elemental arrangement of the LSCT oxygen electrode surface and the chemical composition of the active surface layer (Figure 12).

Figures 12a and 12b demonstrate O 1s spectra for different oxygen electrode materials operated in various environments normalized to peak with lower binding energy. These spectra have two maxima, where a peak at lower binding energy (528.3 eV) is correlated to oxide ions in the lattice, and a peak at higher binding energy (530.8–531.2 eV) is characterizing the surface components like secondary phases and adsorbed oxygen. It can be seen that lattice and surface peak ratios depend on the oxygen electrode material as well as the gas environment. Increasing the amount of Ti^{4+} cations in the B-site of oxygen electrode material, the peak with lower relative intensity indicates that less surface components are formed during operation in contaminated gas compositions at Ti substituted oxygen electrode.

Figures 12c–12f show La 4d and Sr 3d spectra for different oxygen electrode materials working in different gas conditions. These spectra were normalized to La 4d peaks intensities, respectively. The origin of La 4d peaks (101.2 and 103.9 eV) is related to the spin-orbit splitting and crystal field splitting effects. The shape of the Sr 3d signal (131–137 eV) varies depending on the exact composition of the electrode materials and the gas composition. In addition, the full width at half maximum (FWHM) of this structure is much broader than the spin-orbit splitting of the Sr 3d5/2 and Sr 3d3/2 components, which is approximately 1.8 eV. At least two overlapping Sr 3d contributions can be expected with different chemical surroundings [38].

The simplest model applicable contains two different components. The high binding energy region 134–137 eV corresponds to the surface energy component, which characterizes the photoelectron signal from the upper surface region of the sample. The low binding energy region 131–134 eV provides the photoelectron signal from the bulk of the sample. The bulk or the lattice component is regarded as the perovskite structure in the near-surface region. Surface impurities (secondary phases) are generally considered to be surface components [38]. For electrodes operating in synthetic air, the ratio of peak intensities was pretty similar. Still, for electrodes that worked in contaminated gas atmospheres, it can be seen that the peak intensities began to vary more. It can be concluded that in materials operated under CO_2 contaminated gas composition, the change in the shape of Sr 3d photoelectron signal indicates that increasing Ti amount in LSC99 B-site decreases the amount of secondary phases ($SrCO_3$, $Sr(OH)_2$) on the oxygen electrode material surface. For materials that worked under H_2O contaminated gas composition, the change in the surface and bulk signal ratios indicates that increasing the amount of Ti in LSC99 B-site does not positively affect the formation of secondary phases on the oxygen electrode material surface. Based

on XPS data, it can be concluded that doping of LSC99 oxygen electrode B-site with Ti cations improves the material surface stability under a gas atmosphere contaminated with CO_2. Still, no positive effect was observed under H_2O containing gas [16,39,41].

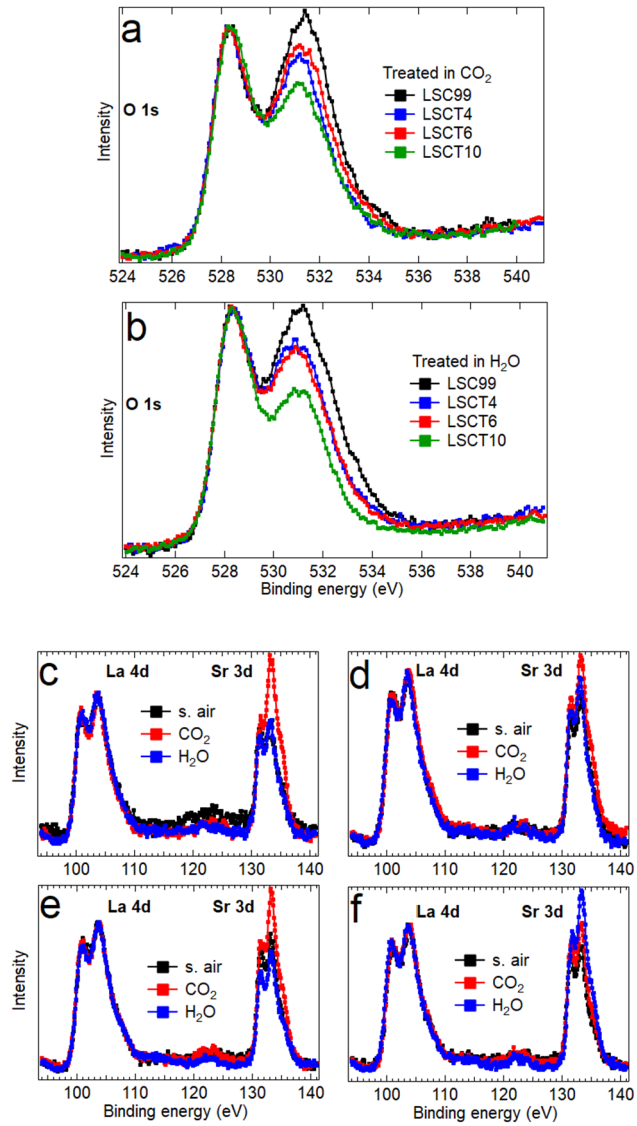

Figure 12. The XPS spectra of 4 samples with different Ti concentrations in the LSC99 B-site, noted in the figure. O 1s spectra (a) for different electrode materials tested in 10% CO_2 in synthetic air and O 1s spectra (b) for different electrode materials tested in 3% H_2O in synthetic air. Spectra of the La 4d, Sr 3d photolines of LSC99 (c), LSCT4 (d), LSCT6 (e), and LSCT10 (f) that have been working in different gas conditions (synthetic air, 10% CO_2 in synthetic air, and 3% H_2O in synthetic air, as shown in the figure).

6.1.6 Time-of-flight secondary ion mass spectrometry analysis of the effect of CO_2 and H_2O on the oxygen electrode materials

TOF-SIMS method was used to analyze the LSC99, LSCT4, LSCT6, and LSCT10 oxygen electrode surface composition and compounds formed on the surface. Based on collected data (Table III), Ti substitution strongly influences the chemical compositions of the electrode surface treated in different gas environments. When comparing oxygen electrodes operated under different environments, synthetic air and CO_2, the Sr concentration on the surface depends on the gas environment applied [74]. It was found that Sr concentration was higher for materials operating under a CO_2 environment than in a synthetic air environment. Adding Ti cations in the LSC99 B-site influences Sr concentration at the surface of the oxygen electrode. Increasing Ti cations content in the B-site decreases Sr concentration at the surface of the electrode. In the case of electrode treatment in the H_2O atmosphere, a small decrease in Sr concentration could be seen if Ti concentration was changed from 0% to 4%. An increase in Ti concentration from 4% to 6% and 10% led to the large increase of Sr concentration on the electrode surface. TOF-SIMS results propose that LSCT10 has the best stability in the CO_2 environment, but LSCT4 was more stable under H_2O contaminated gas environment.

Table III. Element concentrations relative to the sum of the components from the TOF-SIMS measurement of different materials working in different air conditions are noted in the table.

Material and gas phase composition	La (%sum)	Sr (%sum)	Co (%sum)	Ti (%sum)
LSC99 syn. air	11.09	25.84	63.01	0.05
LSC99 CO_2	7.38	55.59	37.02	0.01
LSC99 H_2O	11.05	35.38	53.56	0.01
LSCT4 syn. air	14.68	27.46	56.33	1.53
LSCT4 CO_2	5.85	53.60	39.54	1.01
LSCT4 H_2O	15.16	29.80	53.72	1.32
LSCT6 syn. air	10.66	21.40	45.85	1.75
LSCT6 CO_2	10.42	48.31	39.75	1.52
LSCT6 H_2O	7.34	42.76	47.86	2.05
LSCT10 syn. air	13.86	24.65	44.75	3.77
LSCT10 CO_2	12.15	36.04	48.60	3.20
LSCT10 H_2O	5.57	55.59	36.83	2.02

Materials tested under H_2O conditions do not act similarly to those tested under CO_2 conditions. Presented data visualize the influence of gas components on the Sr segregation magnitude in materials tested. From TOF-SIMS and XPS data, we can expect a complex relationship between the bulk and surface concentrations of elements.

6.2 Electrochemical characterization of oxygen electrode materials

6.2.1 The effect of temperature, oxygen partial pressure, and electrode potential on the oxygen electrode performance

Nyquist plots for studied LSCF and LSC + LSCF materials are given in Figure 13. In Figure 13a, there are normalized Nyquist plots for a better comparison of studied oxygen electrode materials. The value of high-frequency series resistance (when $Z'' = 0$) describes the electrolyte resistance. Lower R_p value obtained for LSC+LSCF indicate that LSC+LSCF is a more active oxygen reduction electrode material. The influence of the temperature to the LSCF oxygen electrode is shown in Figure 13b. Temperature have a significant impact on the ORR kinetics. Figure 14 demonstrates that the LSC and LSCF oxygen electrode powder mixture (LSC+LSCF) has better electrocatalytic activity, and the LSCF has the highest R_p values (Figure 13a). However, the characteristic time constant for ORR depends strongly on the oxygen electrode material chemical composition. Higher absolute phase angle values (φ) have been measured for LSCF compared with the mixture of LSC and LSCF (Figure 14). It can be concluded that LSC+LSCF is a more active oxygen electrode than LSCF.

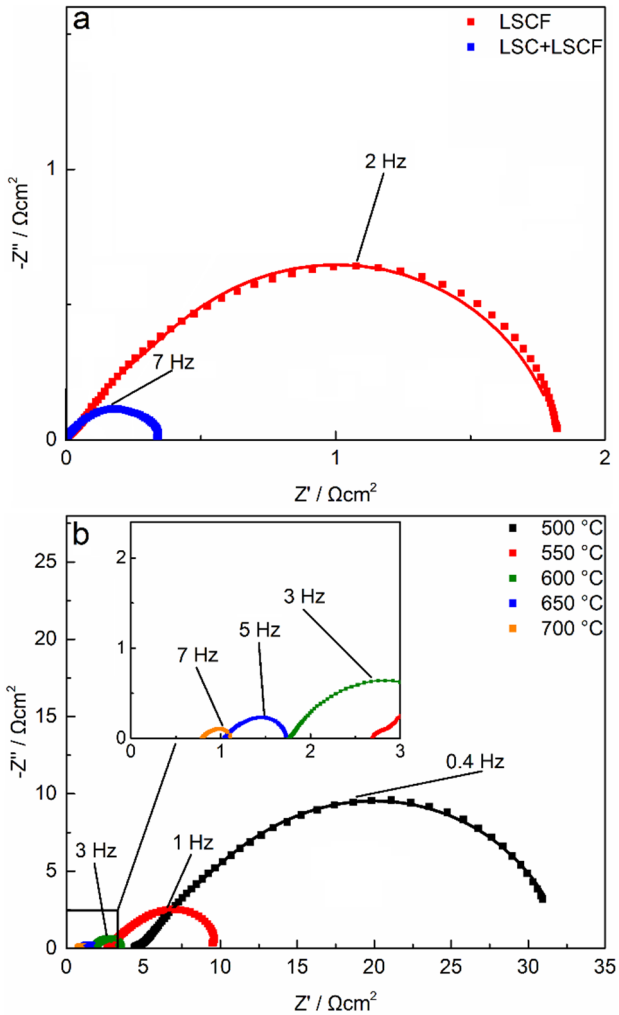

Figure 13. Nyquist plots at T = 600 °C and oxygen electrode potential E = 0 V (vs Pt/porous Pt/O_2) for LSCF and LSC + LSCF (50:50 wt%), noted in the figure (a) and for LSCF at different working temperatures, noted in the figure (b).

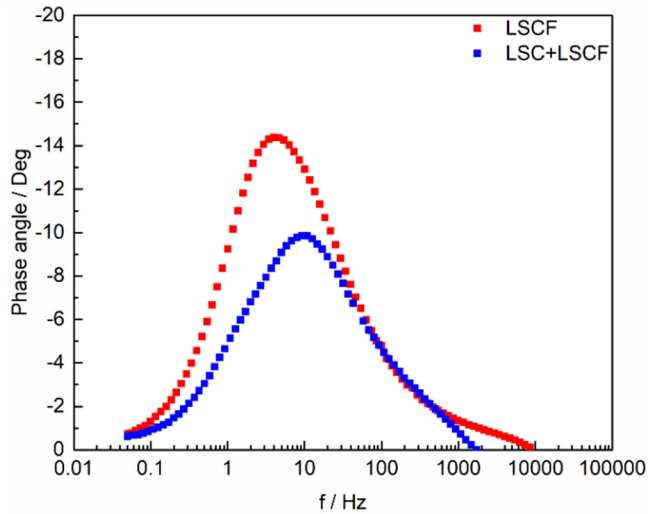

Figure 14. Bode phase angle vs. frequency plots for LSC, LSCF and LSC + LSCF (50:50 wt%) oxygen electrodes (noted in figure) measured in synthetic air at oxygen electrode potential $E = 0$ V (vs. Pt/porous Pt/O_2) and at working temperature $T = 600$ °C.

It can be seen from Figure 15 that negative oxygen electrode potential commences a decrease in R_p values. According to the Butler-Volmer equation, the negative electrode potential improves the ORR rate. Also, the increase of negative potential leads to the rise in the concentration of the defects or vacancies (Figure 6), which also positively affects the speed of total ORR.

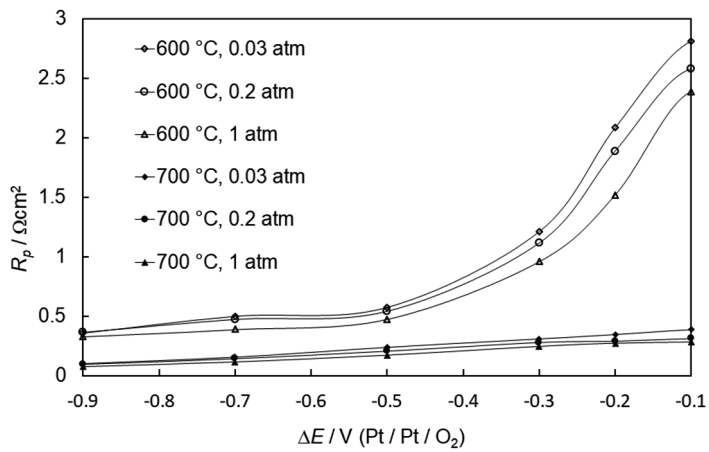

Figure 15. Dependence of polarization resistance (calculated from Nyquist plots) on the LSC oxygen electrode potential at various working temperatures and oxygen partial pressures are noted in the figure.

Figures 15 and 16 show that at 600 °C and lower potential, the total R_p depends on the oxygen partial pressure. More insufficient oxygen partial pressure causes bigger R_p. Even at lower p_{O2} values, the defect, i.e., the active site concentration at the surface, is higher compared to that in a high p_{O2} environment. As it was concluded based on XRD data (Figure 6), the activity of total electrode process is higher at higher p_{O2} and therefore most likely determined by the oxygen activity in the gas phase and not by defect concentration in the oxygen electrode. The data in Figures 15 and 16 also supports this conclusion which shows that the higher experimental R_p values are measured in conditions where the mass transport limitations are typically dominating at lower temperatures and lower gas concentrations.

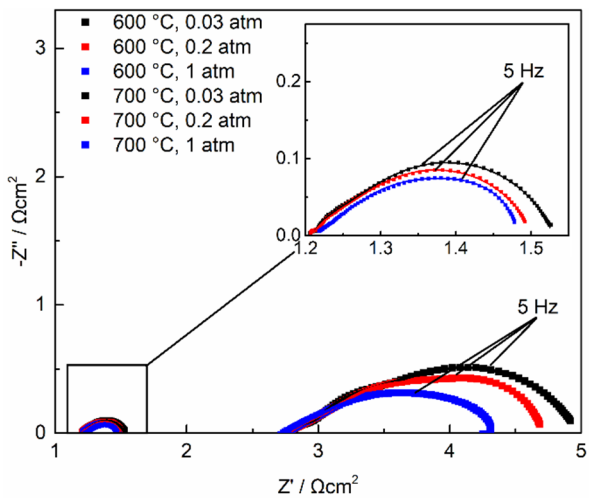

Figure 16. Nyquist plots for LSC were measured at various fixed oxygen partial pressures at multiple working temperatures noted in the figure and fixed electrode potential E = −0.2 V (vs Pt/Pt/O_2).

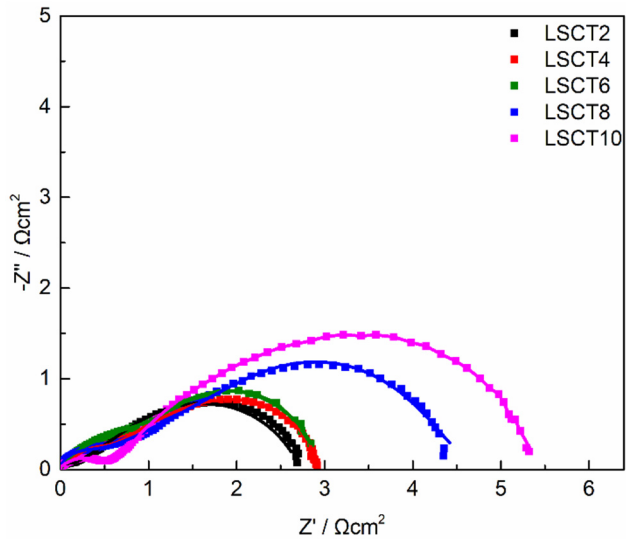

Figure 17. Nyquist plots for the LSCT2, LSCT4, LSCT6, LSCT8, and LSCT10 measured in synthetic air after 200 hours stabilization at oxygen electrode potential $E = -0.1$ V (vs. Pt/porous Pt/O_2) and at working temperature $T = 600$ °C.

Doping LSC99 B-site with Ti cations somewhat decreases the oxygen electrode activity towards ORR (Figure 17). With doping Ti into the B-site of LSC99, the amount of Co cation in the oxide decreases, and therefore, vacancy concentration also decreases. The ORR rate on the perovskite oxygen electrode depends on B-site cations ability to change the oxidation state and the amount of the oxygen vacancies. More oxygen vacancies result in higher activity towards surface reaction. It should be noted that the activities (i.e., polarization resistances) of the oxygen electrode materials presented in this work are not directly comparable because the goal of this work was not to optimize the microstructure of the materials but to show the influence of different contaminants (CO_2, H_2O) in air on the oxygen electrode materials stability and characteristics.

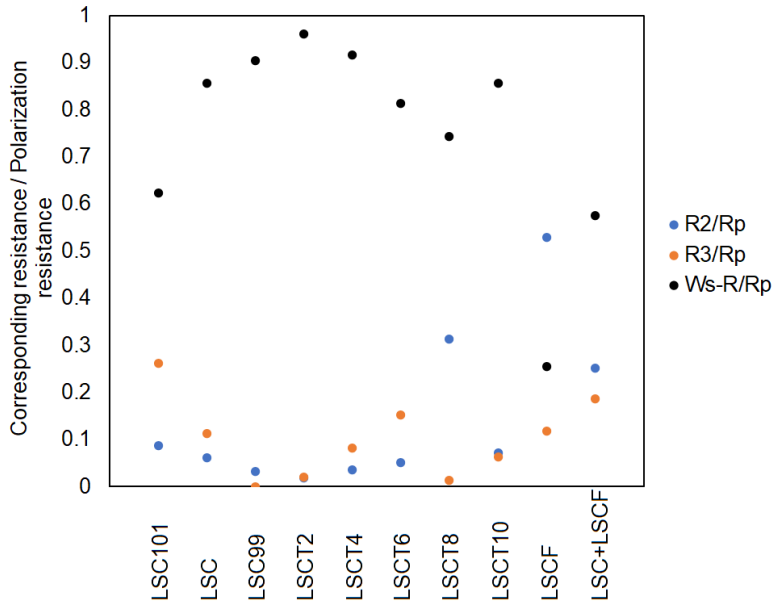

Figure 18. Corresponding EC components contribute to the polarization resistance, R_p, for studied oxygen electrode materials, as noted in the figure. Oxygen electrodes were measured at oxygen electrode potential $E = -0.1$ V (vs. Pt/porous Pt/O_2) and working temperature $T = 600$ °C.

Figure 18 represents impedance data for different oxygen electrode materials. Experimental Nyquist plots have been fitted with EC given in Figure 3. Corresponding EC component resistance values have been divided by R_p to determine their contribution to R_p. It can be found that minor A-site deficiency (LSC99) improves material activity compared to LSC because R_2 and R_3 contributions to the R_p are more negligible than found for LSC. The opposite effect can be seen in the case of LSC101 (A-site excess), where R_2 and R_3 contribute more to R_p. In the case of LSCF, R_2 and R_3 contribution to R_p is more significant, indicating that this material is less active towards ORR. It can be seen that doping of LSC99 B-site with Ti^{4+} cation changes the contribution of high and medium frequency R_2 and R_3 values indicating that the rates of high and medium frequency charge transfer and mass transfer processes are affected. Materials with 8% and 10% Ti^{4+} cations in the LSC99 B-site show a different behavior, which can be explained by a possible change in the material structure described before. It can also be seen that if high or medium frequency processes rates, expressed as resistances R_2 or R_3 contribution increase, then the mass transfer component W_s-R values decrease.

6.2.2 The influence of H_2O and CO_2 concentrations on the oxygen electrode performance

The R_p, calculated from the Nyquist plots [62–64] (Figures 19–21) indicate lower electrochemical activity of the LSC101 oxygen electrode compared to LSC99. LSC101 oxygen electrode material was also more affected by humidified synthetic gas composition than other studied oxygen electrode materials. The data in Figures 19–22 shows that the LSC99 and LSC oxygen electrodes are more active against the ORR than the LSC101 and LSCF electrodes.

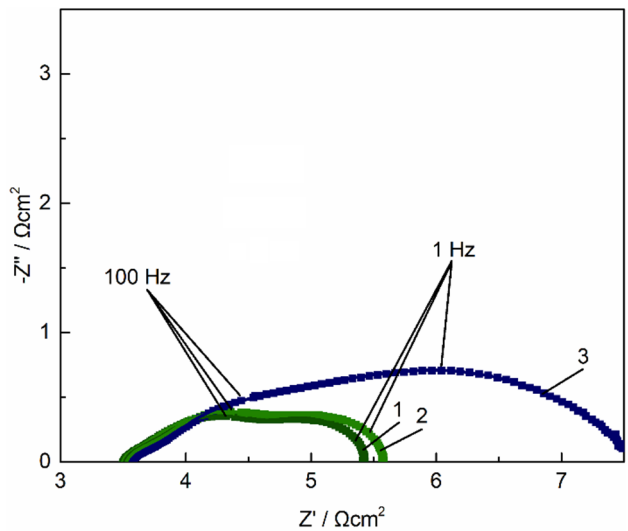

Figure 19. Nyquist plots for the LSC101 were measured at oxygen electrode potential $E = -0.1$ V (vs. Pt/porous Pt/O_2) and at working temperature $T = 650$ °C under various gas feeding conditions 1) at the beginning of the test applying only the dry air, 2) after 10 days of testing in dry air, and 3) after 10 days testing in the humidified synthetic air.

Data in Figure 19 shows that humidified synthetic air has a colossal effect on the rate of LSC 101 oxygen electrode degradation. The oxygen electrode R_p increased nearly 2 times as calculated from the total polarization resistance values. LSC101 R_p increased only by 10% after testing it under synthetic air condition for 10 days. However, testing oxygen electrode under humidified synthetic air conditions for 10 days, degradation of approximately 270% was seen. Interestingly, the very high-frequency R_s does not depend on the conditions, but the R_p resistance increases remarkably. It is probably caused by the formation of $Sr(OH)_2$ at the oxygen electrode surface, thus replacing O^{2-} vacancies with OH^- ions. As the $Sr(OH)_2$ formation occurs on/in the very thin upper layer of the porous oxygen electrode surface, the XRD method was unable to detect possible changes in the LSC oxygen electrode surface structure as there was no big changes within all

oxygen electrode layer. Surprisingly, after the dry synthetic air was fed into the oxygen electrode compartment, the R_p values increased continuously, as demonstrated in Figures 20 and 21. It must be pointed out that for all $La_{0.6}Sr_{0.4}CoO_{3-\delta}$ oxygen electrodes tested, including the LSC101 electrode, the R_p did not decrease after switching back to the dry gas feeding conditions, differently from LSCF (Figure 22), where the remarkable decrease of R_p was measured after switching gas phase back to the dry synthetic air.

The Nyquist plot low-frequency region has been connected with so-called gas phase mass transfer resistance. It can be seen from Figure 20 that this low-frequency region is mainly affected. Both LSC and LSC101 oxygen electrodes have similar dependence. The R_p increases continuously after switching the air phase from the humidified synthetic air back to the dry air.

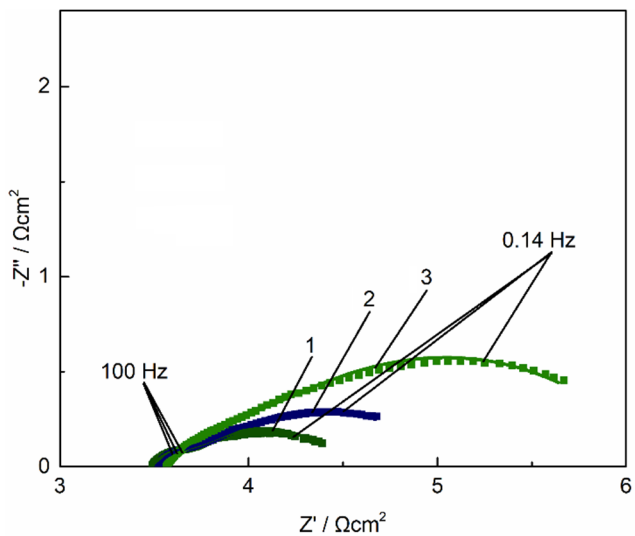

Figure 20. Nyquist plots for the LSC measured at oxygen electrode potential $E = -0.1$ V (vs. Pt/porous Pt/O_2) and at working temperature $T = 700$ °C under various gas feed conditions: 1) at the beginning of the test in dry air, 2) after testing in humidified air for 100 h, and 3) in dry synthetic air, after 100 h polarization in moistured air, and after that testing for 300 h in dry synthetic air.

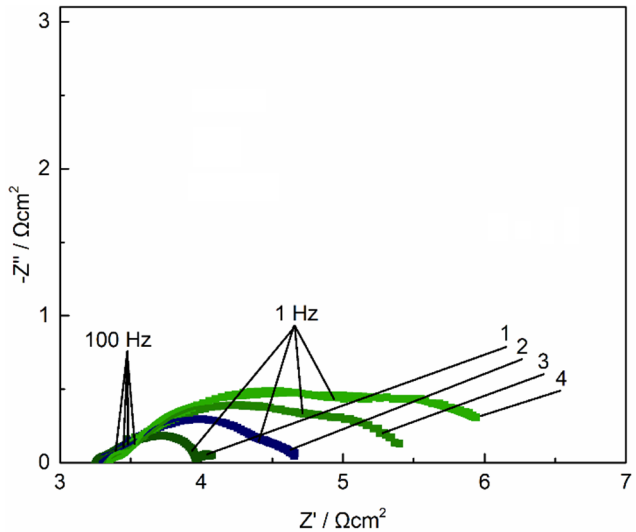

Figure 21. Nyquist plots for the LSC99 were measured at oxygen electrode potential $E = -0.1$ V (vs. Pt/porous Pt/O_2) and at working temperature $T = 650$ °C under various gas feeding conditions: 1) at the beginning of the test in dry air, 2) after testing in humidified air during 100 h, and 3) in dry air, after testing in humidified synthetic air for 250 h, and 4) in dry air, after testing in humidified synthetic air for 320 h.

LSCF oxygen electrodes behave differently from LSC and LSC101 oxygen electrodes (Figure 22). An increase of R_p has been established after feeding the electrode compartment with humidified synthetic air for 80h. Switching back to dry synthetic air, the R_p decreases, but the process is not totally complete, i.e., degradation is not fully reversible. It can also be concluded that the high-frequency part of the Nyquist plot is unaffected, meaning that the rate of the faradic charge transfer and the total charge transfer process does not change. It all leads to understanding that the limiting process for ORR in our studied oxygen electrodes is the mass transfer processes in meso-microporous structure.

The formation kinetics of OH^- depends strongly on the B-site cation's capability to change its oxidation state. Because cobalt changes its oxidation state more quickly than iron cations, the amount of the oxide ions decreased faster for LSC oxygen electrodes. OH^- anions appear only in the upper layers of the oxygen electrode, and the bulk lattice is more firm because Co^{4+} has been partially reduced to Co^{3+}, so O^{2-} diffusion is disabled.

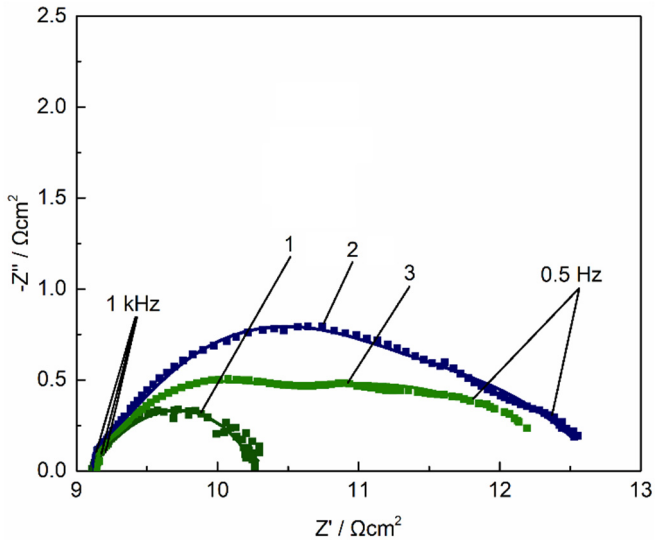

Figure 22. Nyquist plots for the LSCF measured at oxygen electrode potential $E = -0.1$ V (vs. Pt/porous Pt/O_2) and at working temperature $T = 700$ °C under various gas feed conditions 1) at the beginning of the test in dry air, 2) after 80 h in humidified air, and 3) in dry air for 100h after testing in humidified air.

The Nyquist plots in Figure 23 show that after testing the Ti^{4+} cations substituted electrode for 50 h in humidified synthetic air, the R_p values for the electrode have increased only slightly. After replacing the gas environment with synthetic air, the R_p values remain the same for LSCT2, LSCT4, LSCT6, and LSCT8 under humidified synthetic air conditions. Only for LSCT10, the electrochemical degradation continues after moving the gas compartment back to the dry synthetic air. It was shown previously how humidified gas influences the activity of LSC oxygen electrode material and that the doping of B-site with Ti^{4+} improves the electrode material durability against humidity. For materials with Ti^{4+} content 2%, 4%, 6%, and 8%, the increase of R_p was minimal, i.e., if the concentration is lower than 10%. Minor degradation is probably caused by the formation of the $Sr(OH)_2$ layer at the oxygen electrode surface.

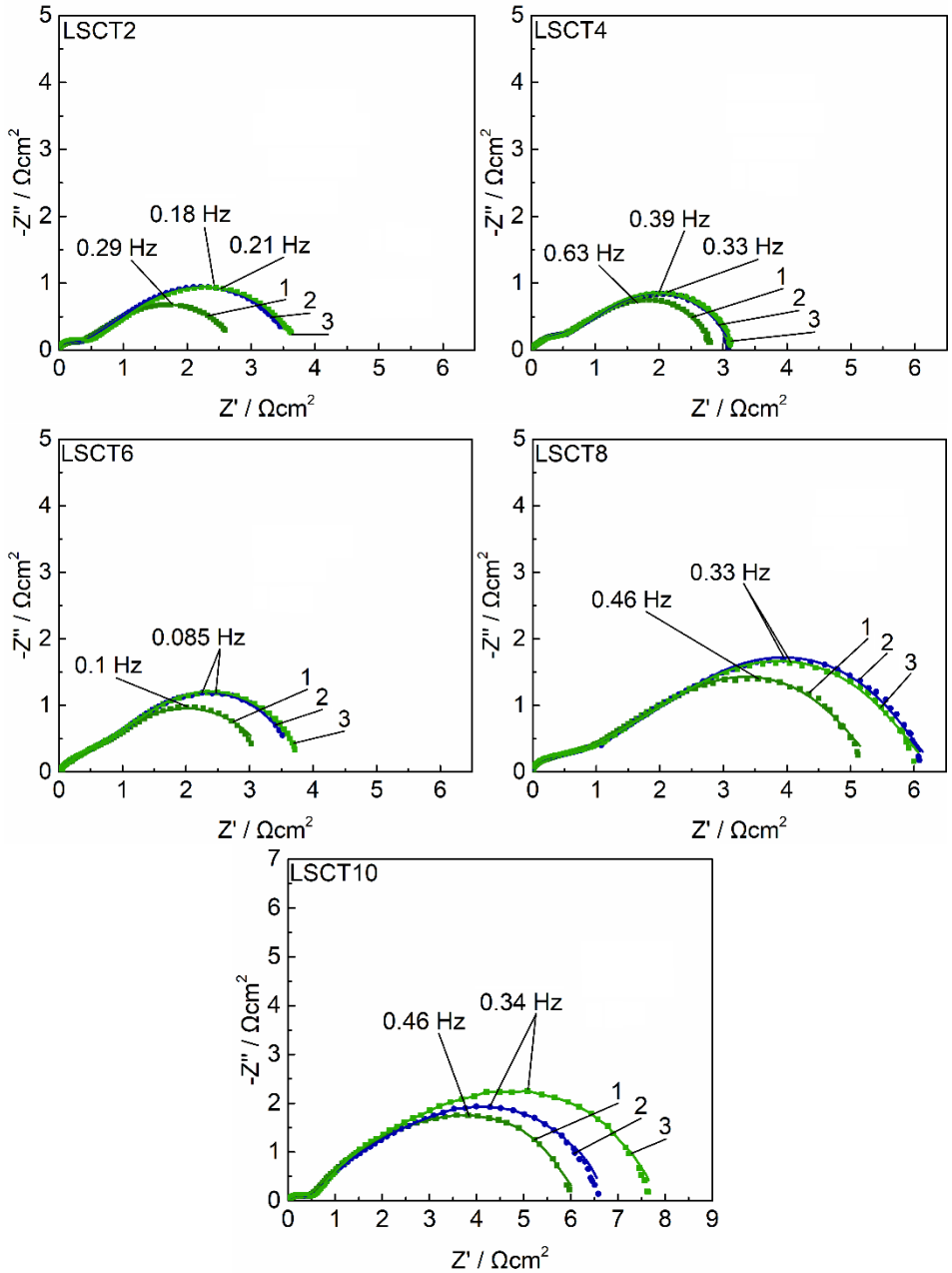

Figure 23. Nyquist plots for the studied materials (compositions presented in figure), at working temperature T = 600 °C and at oxygen electrode potential E = −0.1 V (vs. Pt/porous Pt/O_2). The numbers on curves refer to various gas feeding conditions: 1) at the beginning of the test in synthetic air, 2) after testing in the air with 3% H_2O addition during 50 h, 3) after 50 h polarization in synthetic air.

In Figure 24 the impedance data for LSC99 oxygen electrode material measured in different gas conditions is given. It can be seen that when CO_2 is added to the gas compartment, then R_p values increase. When switching back to CO_2-free synthetic air, R_p values are still increasing. This indicates that degradation continues. For materials with Ti^{4+} cation in the B-site, it can be concluded that Ti^{4+} cation addition improves the material stability against CO_2 (Figure 25). Materials with 2% and 4% Ti^{4+} in the B-site show reversible degradation. Firstly R_p values increase when CO_2 is introduced into the gas mixture, and when switching back to synthetic air, R_p values decrease almost back to the initial value. Also, the increase of the R_p is not as significant compared to unmodified material when CO_2 is introduced into the gas compartment.

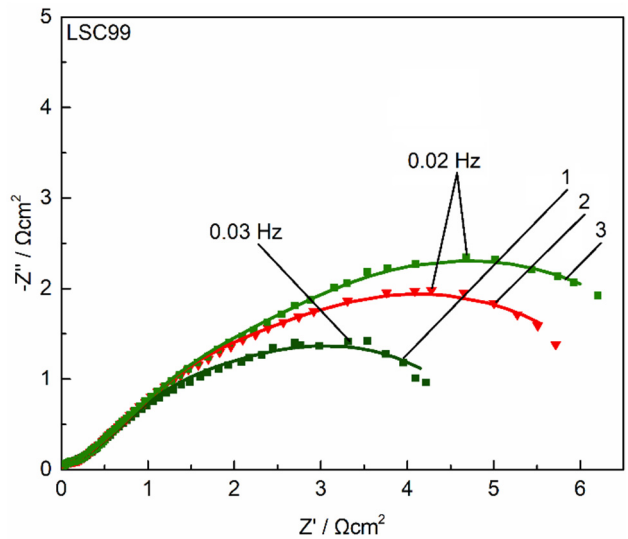

Figure 24. Nyquist plots for the LSC99, at working temperature $T = 600$ °C and at oxygen electrode potential $E = -0.1$ V (vs. Pt/porous Pt/O_2), measured under various gas feeding conditions: 1) at the beginning of test in synthetic air, 2) after testing in the air with 10% CO_2 addition during 100 h and 3) after 50 h polarization in synthetic air.

For materials with 6% and 8% Ti in the B-site, the degradation is also partially reversible. After testing under CO_2 contaminated conditions and switching back to synthetic air, R_p values decrease, but R_p values do not obtain the initial value. For material with 10% Ti in the B-site, the degradation is not reversible, but after switching back to the synthetic air, R_p remains the same for 50 hours.

Materials that showed reversible degradation the degradation process could be described with CO_2 molecules blocking adsorption onto the active sites, whereas the low-frequency part of the Nyquist plot is mainly affected. CO_2 molecules occupy active sites on the surface, which is expressed with the increase

of the low-frequency part of the R_p. The low-frequency part of the Nyquist plot describes mainly the slow gas-phase transport limitations. For materials under study, if CO_2 adorbs/absorbs into the perovskite, then both monodentate and/or unidentate and bidentate carbonates are formed. Monodentate carbonates form when C atoms of CO_2 bond with basic O^{2-} ion in the perovskite structure. If C in CO_2 atoms are bonding with basic O^{2-} ion in perovskite and O atoms of CO_2 connect with the oxygen vacancy in perovskite, then the surface bidentate carbonate species are formed [75].

The Nyquist plot high-frequency part is characteristic of the mixed kinetic processes in electrode macropores and faradic charge transfer limited processes at open surface areas [76]. Conducted electrochemical measurements show (Figure 26) that the effect of CO_2 on the high-frequency part of impedance depends on the Ti^{4+} cation concentration in the electrode material. Figure 26 shows that the contribution of limiting processes are changing for different chemical compositions. For materials with 2 % and 10 % Ti^{4+} cations in the B-site, the high-frequency semi-circle can be seen, but for materials with 4 %, 6 %, and 8 % Ti^{4+} cations in the B-site, limiting processes are changing, and the semi-circle in the frequency region from 600 Hz to 18000 Hz cannot be observed. It can also be seen that limiting process resistance in the 1000 Hz and 100 Hz range decreases with CO_2 addition for material with 10 % Ti^{4+} cations in the B-site. It shows that mentioned processes are accelerated. For other materials, CO_2 does not significantly affect the high-frequency process rate. For other materials, this kind of effect is not so clear. For materials with 2% and 4% Ti^{4+} cations substitution in B-site, it can also be seen that switching back to synthetic air after CO_2 treatment (addition in synthetic air), the high-frequency part remains the same, and no future degradation of oxygen electrode material takes place.

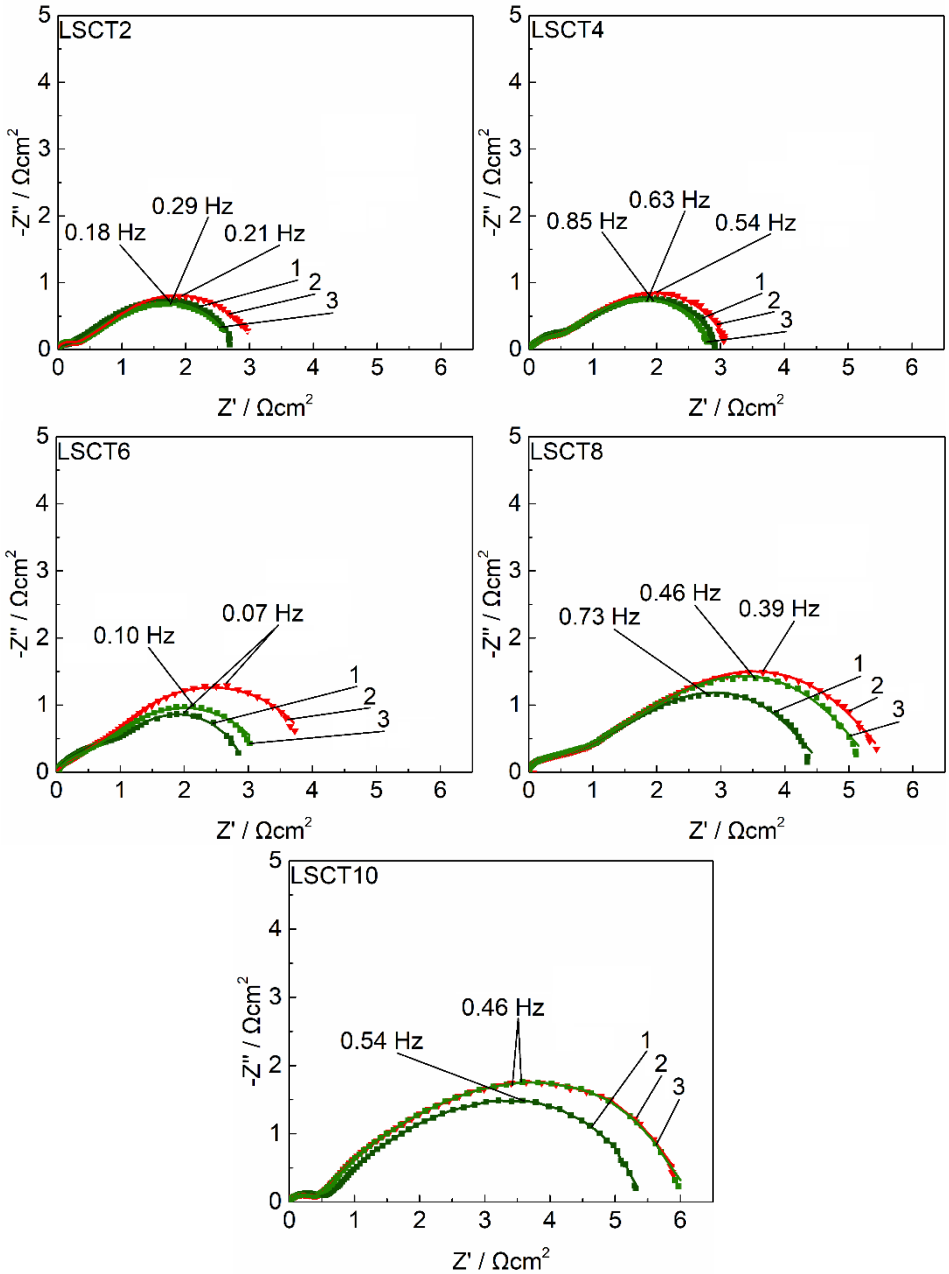

Figure 25. Nyquist plots for the studied materials (compositions presented in the figure) at working temperature T = 600 °C and at oxygen electrode potential E = −0.1 V (vs. Pt/porous Pt/O_2). The numbers on the curves refer to various gas feeding conditions: 1) at the beginning of the test in synthetic air, 2) after testing in the air with 10% CO_2 addition during 100 h, and 3) after 50 h polarization in synthetic air.

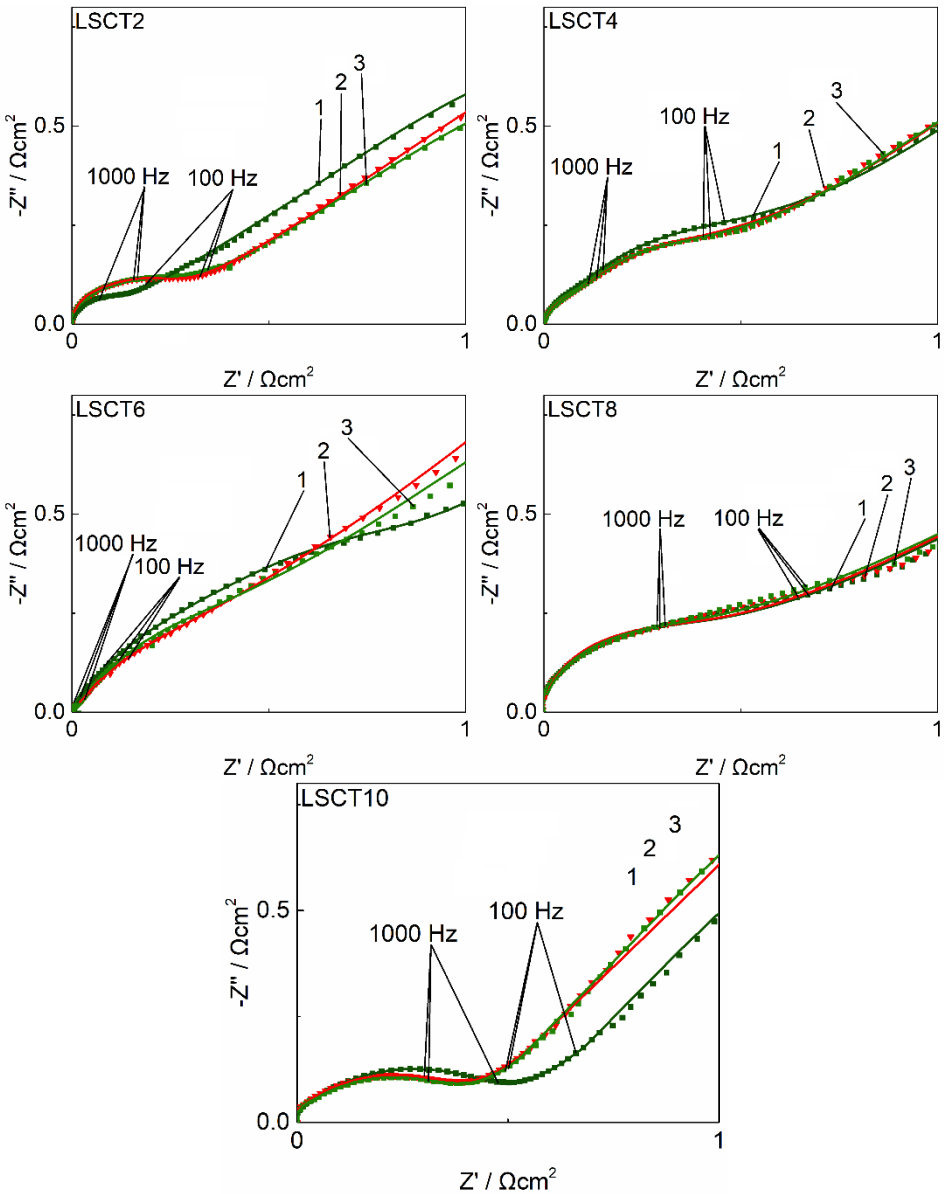

Figure 26. High-frequency semi-circle areas of Nyquist plots for the studied materials (compositions presented in the figure), at working temperature $T = 600$ °C and at oxygen electrode potential $E = -0.1$ V (vs. Pt/porous Pt/O_2). The numbers on the curves refer to various gas feeding conditions: 1) at the beginning of the test in synthetic air, 2) after testing in the air with 10% CO_2 addition during 100 h, and 3) after 50 h polarization in synthetic air.

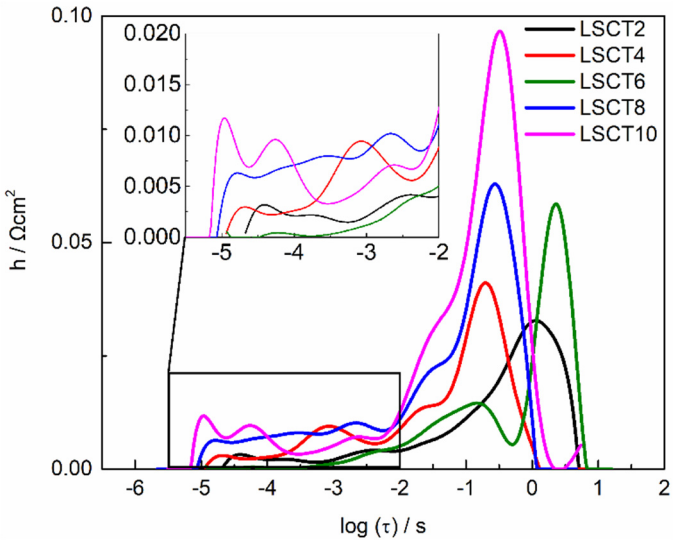

Figure 27. Distribution of relaxation times for studied LSCT oxygen electrode materials, measured in synthetic air at working temperature T = 600 °C and at oxygen electrode potential E = −0.1 V (vs. Pt/porous Pt/O_2).

Figure 27 represents DRT data for studied LSCT oxygen electrode materials analyzed with EC-IDEA software [59,60]. It can be seen that 3 different processes take place in the high-frequency range (f > 100 Hz) and at least two processes at lower frequencies. It also coincides with information gained from Nyquist plots (Figure 24) that on high and medium frequency ranges, there are multiple various processes, and the electrode composition influences them.

Micro-mesoporous oxygen electrode structure can be seen in Figure 28. Only SEM images for LSCT4 in the region where SEM resolution can be used to visualize 3D structure are presented because all the materials tested had similar porous non-homogeneous microstructures. The picture shows that after being tested in different environments, they all look identical, indicating that CO_2 or H_2O addition to synthetic air does not significantly affect the microstructure of the oxygen electrode materials.

Very surface-sensitive FIB-TOF-SIMS data indicates that there are different surface thin-film oxide layers at electrode surface after long testing under electrochemical polarization in CO_2 and H_2O containing air gas phase.

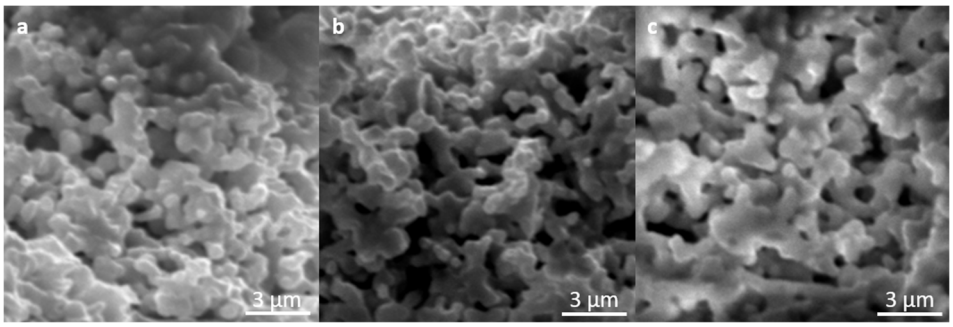

Figure 28. The SEM images of cross-sections of studied oxygen electrodes were tested for 100h in different conditions: a) synthetic air, b) 10% CO_2 in synthetic air, and c) 3% H_2O in synthetic air.

7. SUMMARY

$(La_{0.6}Sr_{0.4})_yCoO_{3-\delta}$, $La_{0.6}Sr_{0.4}Co_{0.2}Fe_{0.8}O_{3-\delta}$ and $(La_{0.6}Sr_{0.4})_{0.99}Co_{1-x}Ti_xO_{3-\delta}$ perovskite-based oxygen electrode materials were prepared and characterized as a potential solid oxide cell oxygen electrodes. Oxygen reduction process kinetics from various gas phase compositions (clean and dry artificial air, wet air, CO_2 contaminated artificial air) have been tested at perovskite-type electrodes.

In situ HT-XRD measurement showed that negative oxygen electrode potential, temperature, and oxygen partial pressure have a reversible influence on the crystallographic cell volume of studied $La_{0.6}Sr_{0.4}CoO_{3-\delta}$, $La_{0.6}Sr_{0.4}Co_{0.2}Fe_{0.8}O_{3-\delta}$ and $La_{0.6}Sr_{0.4}CoO_{3-\delta}$ + $La_{0.6}Sr_{0.4}Co_{0.2}Fe_{0.8}O_{3-\delta}$ electrode materials. The change in crystallographic unit cell volume is caused by the formation of oxygen vacancies and the change in the oxidation state of the B-site cation introduced.

From thermogravimetric analysis and electrochemical impedance data, it can be concluded that doping of the B-site of $(La_{0.6}Sr_{0.4})_{0.99}CoO_{3-\delta}$ with Ti^{4+} ion increases material stability during the thermal cycle. Mass change during the thermal cycle is smaller for B-site modified materials, indicating that the oxygen vacancy formation is less extensive. Time-of-flight secondary ion mass spectrometry and X-ray diffraction analysis results showed that material modification with Ti^{4+} ions reduced Sr segregation onto the electrode surface. Therefore, enhanced stability against H_2O and CO_2 has been achieved.

From electrochemical impedance data it was found that the decrease of the oxygen electrode negative potential causes some increase in the total polarization resistance. Also, at lower oxygen partial pressure, the negative oxygen electrode potential has a more significant effect on the polarization resistance values, which could be explained by the lower oxygen chemical potential in the gas phase.

The influence of the CO_2 and H_2O on the oxygen electrode material activity was also observed with electrochemical impedance spectroscopy. It can be concluded that $La_{0.6}Sr_{0.4}CoO_{3-\delta}$, $(La_{0.6}Sr_{0.4})_{0.99}CoO_{3-\delta}$ and $(La_{0.6}Sr_{0.4})_{1.01}CoO_{3-\delta}$ oxygen electrode material degradation accelerated if H_2O additions were introduced into the electrode compartment. It was established that the polarization resistance started to increase. The degradation observed for these materials was not reversible. After the H_2O contaminated gas was changed back to the dry synthetic air, polarization resistance continued to increase. However, it was noticed that a slight deficiency in the A-site for $(La_{0.6}Sr_{0.4})_{0.99}CoO_{3-\delta}$ improves the stability of the perovskite structure.

The Fe cations substituted $La_{0.6}Sr_{0.4}Co_{0.2}Fe_{0.8}O_{3-\delta}$ oxygen electrode material showed somewhat different behavior than the above materials. Switching back to dry synthetic air after contaminated gas was directed into the gas compartment caused a decrease in polarization resistance, indicating that reversible degradation of $La_{0.6}Sr_{0.4}Co_{0.2}Fe_{0.8}O_{3-\delta}$ took place.

Humidity has a different effect on Ti^{4+} cations substituted $(La_{0.6}Sr_{0.4})_{0.99}Co_{1-x}Ti_xO_{3-\delta}$ materials. Humidity affects also $(La_{0.6}Sr_{0.4})_{0.99}Co_{0.98}Ti_{0.02}O_{3-\delta}$,

$(La_{0.6}Sr_{0.4})_{0.99}Co_{0.96}Ti_{0.04}O_{3-\delta}$, $(La_{0.6}Sr_{0.4})_{0.99}Co_{0.94}Ti_{0.06}O_{3-\delta}$ oxygen electrode material degradation. H_2O addition increases the degradation rate, but after switching back to dry synthetic air, degradation stops for at least 50 hours.

Materials with more higher Ti^{4+} cations concentration in the B-site, like $(La_{0.6}Sr_{0.4})_{0.99}Co_{0.92}Ti_{0.08}O_{3-\delta}$, $(La_{0.6}Sr_{0.4})_{0.99}Co_{0.90}Ti_{0.10}O_{3-\delta}$ behaved similarly to $La_{0.6}Sr_{0.4}CoO_{3-\delta}$, $(La_{0.6}Sr_{0.4})_{0.99}CoO_{3-\delta}$ and $(La_{0.6}Sr_{0.4})_{1.01}CoO_{3-\delta}$ oxygen electrode material.

CO_2 addition in synthetic air also negatively affects the $(La_{0.6}Sr_{0.4})_{0.99}CoO_{3-\delta}$ oxygen electrode material stability, increasing degradation rate. Also, the degradation is not reversible, meaning that degradation continues after switching gas-phase composition back to clean synthetic air. It should be stressed that improved stability was observed for all materials modified with Ti^{4+} cations. $(La_{0.6}Sr_{0.4})_{0.99}Co_{0.98}Ti_{0.02}O_{3-\delta}$, $(La_{0.6}Sr_{0.4})_{0.99}Co_{0.96}Ti_{0.04}O_{3-\delta}$, showed improved stability and fully reversible degradation. CO_2 addition increases the degradation rate, but polarization resistance value decreases back to its initial value after switching gas-phase composition back to clean synthetic air. Partially reversible degradation was observed for $(La_{0.6}Sr_{0.4})_{0.99}Co_{0.94}Ti_{0.06}O_{3-\delta}$ and $(La_{0.6}Sr_{0.4})_{0.99}Co_{0.92}Ti_{0.08}O_{3-\delta}$. For $(La_{0.6}Sr_{0.4})_{0.99}Co_{0.90}Ti_{0.10}O_{3-\delta}$ addition of CO_2 into the gas phase increases the degradation rate, but degradation stops after switching back to dry synthetic air.

Thus, the Ti^{4+} substituted perovskites are promising materials for application in solid oxide devices under study at the University of Tartu Institute of chemistry.

8. REFERENCES

[1] N. Q. Minh, T. Takahashi, Science and Technology of Ceramic Fuel Cells, Elsevier, Amsterdam 1995.
[2] S.C. Singhal, K. Kendall, High Temperature Solid oxide Fuel Cells: Fundamentals, Design and Applications, Elsevier, Amsterdam 2003.
[3] D.A.J. Rand, R.M. Dell, Hydrogen Energy: Challenges and Prospects, Royal Society of Chemistry, Cambridge 2007.
[4] M. Mogensen, Current Opinion in Electrochemistry 21 (2020) 265–273.
[5] F. Bidrawn, G. Kim, N. Aramrueang, J. M. Vohs, R. J. Gorte, J. Power Sources 195 (2010) 720–728.
[6] M. Mogensen, D. Lybye, N. Bonanos, P. V. Hendriksen, F. W. Poulsen, Solid State Ionics 174 (2004) 279–286.
[7] S. P. Jiang, J. Hydrogen Energy 44 (2019) 7448–7493.
[8] Y. Chen, S. Yoo, Y. Choi, J. H. Kim, Y. Ding, K. Pei, R. Murphy, Y. Zhang, B. Zhao, W. Zhang, H. Chen, Y. Chen, W. Yuan, C. Yang, M. Liu, Energy Environ. Sci. 11 (2018) 2458–2466.
[9] I. Kivi, J. Aruväli, K. Kirsimäe, P. Möller, A. Heinsaar, G. Nurk, E. Lust, J. Solid State Electrochem 21 (2017) 361–369.
[10] B. Koo, K. Kim, J. K. Kim, H. Kwon, J. W. Han, W. Jung, Joule 2 (2018) 1476–1499.
[11] H. Ding, A. V. Virkar, M. Liu, F. Liu, Phys. Chem. Chem. Phys. 15 (2013) 489–496.
[12] W. Lee, J.W. Han, Y. Chen, Z. Cai, B. Yildiz, J. Am. Chem. Soc. 135 (2013) 7909–7925.
[13] S. Y. Lai, D. Ding, M. Liu, M. Liu, F. M. Alamgir, ChemSusChem. 7 (2014) 3078–3087.
[14] N. Tsvetkov, Q. Lu, L. Sun, E. J. Crumlin, B. Yildiz, Nat. Mater. 15 (2016) 1010–1016.
[15] T. Nagai, W. Ito, T. Sakon, Solid State Ionics 177 (2007) 3433–3444.
[16] X. Chen, S. P. Jiang, J. Mater. Chem. A. 1 (2013) 4871–4878.
[17] M. Li, M. Zhao, F. Li, W. Zhou, V. K. Peterson, X, Xu, Z. Shao, I. Gentle, Z. Zhu, Nat. Commun. 8 (2017) 13990.
[18] S. M. Fang, C. Y. Yoo, H. J. M. Bouwmeester, Solid State Ionics 195 (2011) 1–6.
[19] J.T.S. Irvine, P. Connor, Solid Oxide Fuels Cells: Facts and Figures, Springer, London 2013.
[20] A. Weber, E. Ivers-Tiffée, J. Power Sources 127 (2004) 273–283.
[21] S. C. Singhal, WIREs Energy Environ 3 (2014) 179–194.
[22] C. Sun, R. Hui, J. Roller, J. Solid State Electrochem 14 (2010) 1125–1144.
[23] A. M. Glazer, Acta Crystallogr. Sect. B 28 (1972) 3384–3392.
[24] I. Yasuda, K. Ogaswara, M. Hishinuma, T. Kawada, M. Dokiya, Solid State Ionics 86–88 (1996) 1197–1201.
[25] D. J. L. Brett, A. Atkinson, N. P. Brandon, S. J. Skinner, Chem. Soc. Rev. 37 (2008) 1568–1578.
[26] A. Petric, P. Huang, F. Tietz, Solid State Ionics 135 (2000) 719–725.
[27] H. Ullmann, N. Trofimenko, F. Tietz, D. Stöver, A. Ahmad-Khanlou, Solid State Ionics 138 (2000) 79–90.
[28] S. Ya. Istomin, E. V. Antipov, Russ. Chem. Rev. 82 (2013) 686–700.

[29] F. Tietz, Ionics 5 (1999) 129–139.
[30] E. Y. Konysheva, X. Xu, J. T. S. Irvine, Adv. Mater. 24 (2012) 528–532.
[31] K. K. Hansen, Mater Res Bull. 45 (2010) 197−199.
[32] Y. Zhu, W. Zhou, J. Yu, Y. Chen, M. Liu, Z. Shao, Chem. Mater. 28 (2016) 1691−1697.
[33] Y. Zhu, Z.-G. Chen, W. Zhou, S. Jiang, J. Zou, Z. Shao, ChemSusChem 6 (2013) 2249−2254.
[34] Y. Yu, H. Luo, D. Cetin, X. Lin, K. Ludwig, U. Pal, S. Gopalan, S. Basu, Applied Surface Science 323 (2014) 71−79.
[35] B. Koo, K. Kim, J. K. Kim, H. Kwon, J. W. Han, W. Jung, Joule 2 (2018) 1476−1499.
[36] H. Ding, A. V. Virkar, M. Liu, F. Liu, Phys. Chem. Chem. Phys. 15 (2013) 489−496.
[37] W. Lee, J. W. Han, Y. Chen, Z. Cai, B. Yildiz, J. Am. Chem. Soc. 135 (2013) 7909−7925.
[38] S. Y. Lai, D. Ding, M. Liu, M. Liu, F. M. Alamgir, ChemSusChem 7 (2014) 3078−3087.
[39] N. Tsvetkov, Q. Lu, L. Sun, E. J. Crumlin. B. Yildiz, Nat. Mater. 15 (2016) 1010−1016.
[40] S. Kim, J. Ryu, H. Lee, Advances in Applied Ceramics 117 (2018) 155−160.
[41] T. Nagai, W. Ito, T. Sakon, Solid State Ionics 177 (2007) 3433−3444.
[42] M. Li, M. Zhao, F. Li, W. Zhou, V. K. Peterson, X. Xu, Z. Shao, I. Gentle, Z. Zhu, Nat. Commun. 8 (2017) 13990.
[43] J. Richter, P. Holtappels, T. Graule, T. Nakamura, J. L. Gauckler, Monatshefte für Chemie 140 (2009) 985−999.
[44] J. Sunaraso, S. S. Hashim, N. Zhu, W. Zhou, Progress in Energy and Combustion Science 61 (2017) 57−77.
[45] H. Kozuka, K. Ohbayashi, K. Koumoto, Sci. Technol. Adv. Mater. 16 (2015) 026001.
[46] P. M. Woodward, Acta Cryst. B53 (1997) 32−42.
[47] W. Chaibi, R. Pelaez, C. Blondel, C. Drag, C. Delasart, Eur. Phys. J. D 58 (2010) 29−37.
[48] J. E. Huuhey et al., Inorganic Chemistry, 4th ed. (New York: HarperCollins, 1993)
[49] E. Barsoukov, J.R. Macdonald, Impedance Spectroscopy: Theory, Experiment, and Applications, 2nd ed., John Wiley & Sons, New Jersey 2005.
[50] S. McIntosh, R.J. Gorte, Chem. Rev. 104 (2004) 4845–4866.
[51] J. Winkler, P. V. Hendriksen, N. Bonanos, M. Mogensen, J. Electrochem. Soc. 145 (1998) 1184−1192.
[52] S. B. Adler, J. Electrochem. Soc. 149 (2002) E166.
[53] S. McIntosh, J. M. Vohs, R. J. Gorte, J. Electrochem. Soc. 150 (2003) A1305.
[54] I. Scribner Associates, ZView Operating Manual, Scribner Associates, Inc, 2016.
[55] A. Lasia, Electrochemical Impedance Spectroscopy and Its Applications in Modern Aspects of Electrochemistry, Kluwer Academic/Plenum Publishers, New York, 1999.
[56] E. Lust, G. Nurk, S. Kallip, I. Kivi, P. Möller, J. Solid State Electrochemistry 9 (2005) 674−683.
[57] E. Lust, P. Möller, I. Kivi, G. Nurk, S. Kallip, P. Nigu, K. Lust, J. Electrochem. Soc. 152 (2005) A2306−A2308.
[58] S. Dierickx, A. Weber, E. Ivers-Tiffee, Electrochim. Acta 355 (2020) 136764.

[59] M. Hahn, S. Schindler, L.–C. Triebs, M. A. Danzer, Batteries 5 (2019) 43.
[60] M. A. Danzer, Batteries 5 (2019) 53.
[61] L. E. Smart, E. A. Moore, Solid State Chemistry: An Introduction, 3rd Edition, CRC Press, Boca Raton 2005.
[62] E. Lust, R. Küngas, I. Kivi, H. Kurig, P. Möller, E. Anderson, K. Tamm, A. Samussenko, K. Lust, G. Nurk, Electrochim. Acta 55 (2010) 7669–7678.
[63] R. Küngas, I. Kivi, E. Lust, J. Electrochem. Soc. 156 (2009) B345–B352.
[64] R. Küngas, I. Kivi, K. Lust, G. Nurk, E. Lust, J. Electroanal. Chem. 629 (2009) 94–101.
[65] P. Hjalmarsson, M. Søgaard, A. Hagen, M. Mogensen, Solid State Ionics 179 (2008) 636–646.
[66] A. N. Petrov, O. F. Kononchuk, A. V. Andreev, V. A. Cherepanov, P. Kofstad, Solid State Ionics 80 (1995) 189–199.
[67] S. Estemirova, A. Fetisov, V. Balakirev S. Titova, J. Supercond. Nov. Magn. 20 (2007) 113–116.
[68] K. Chen, S. He, N. Li, Y. Cheng, N. Ai, M. Chen, W. D. A. Ricard, T. Zhang, S. P. Jiang, J. Power Sources 378 (2018) 433–442.
[69] K. E. Sickafus, J. A. Valdez, J. R. Williams, R. W. Grimes, H. T. Hawkins, Nuclear Instruments and Methods in Physics Research B 191 (2002) 549–558.
[70] S. Hashimoto, Y. Fukuda, M. Kuhn, K. Sato, K. Yashiro, J. Mizusaki, Solid State Ionics 186 (2011) 37–43.
[71] M. Søgaard, P. V. Hendriksen, M. Mogensen, F. W. Poulsen, and E. Skou, Solid State Ionics 177 (2006) 3285–3296.
[72] M. M. Kuklja, E. A. Kotomin, R. Merkle, Yu. A. Mastrikov, J. Maier, Phys. Chem. Chem. Phys. 15 (2013) 5443–5471.
[73] F. Wang, T. Nakamura, K. Yashiro, J. Mizuaki, K. Amezawa, Solid State Ionics 262 (2014) 719–723.
[74] X. Wang, Ziye Pan, X. Chu, K. Huang, Y. Cong, R. Cao, R. Sarangi, L. Li, G. Li, S. Feng, Angew. Chem. Int. Ed. 58 (2019) 11720–11725.
[75] K. Coenen, F. Gallucci, B. Mezari, E. Hensen, M. van S. Annaland, J.CO2 Utilization 24 (2018) 228–239.
[76] Q. A. Huang, R. Hui, B. Wang, J. Zhang, Electrochim. Acta, 52 (2007) 8144–8164.

9. SUMMARY IN ESTONIAN

Kõrgtemperatuurse tahkeoksiidelemendi hapnikelektroodimaterjalide uurimine realistlikes töötingimustes

Antud doktoritöös valmistati ja uuriti $(La_{0.6}Sr_{0.4})_yCoO_{3-\delta}$, $La_{0.6}Sr_{0.4}Co_{0.2}Fe_{0.8}O_{3-\delta}$ ja $(La_{0.6}Sr_{0.4})_{0.99}Co_{1-x}Ti_xO_{3-\delta}$ perovskiitse kristallstruktuuriga materjale, mis on potentsiaalsed kõrgtemperatuurse tahkseoksiid kütuseelemendi hapnikelektroodi materjalid. Uuriti erinevate gaasi faasi koostiste (kuiv ja puhas sünteetiline õhk, niisutatud sünteetiline õhk, CO_2 lisandiga sünteetiline õhk) mõju nimetatud hapnikelektroodide stabiilsusele.

In situ kõrgtemperatuurse röntgendifraktsiooni mõõtmised näitasid, et hapnikelektroodi negatiivsel potentsiaalil, temperatuuril ja hapniku osarõhul on pöörduv mõju uuritud $La_{0.6}Sr_{0.4}CoO_{3-\delta}$, $La_{0.6}Sr_{0.4}Co_{0.2}Fe_{0.8}O_{3-\delta}$ ja $La_{0.6}Sr_{0.4}CoO_{3-\delta}$ + $La_{0.6}Sr_{0.4}Co_{0.2}Fe_{0.8}O_{3-\delta}$ hapnikelektroodi materjalide kristallograafilistele ühikraku parameetritele. Ühikraku ruumala muutus on põhjustatud B-asendi katiooni oksüdatsiooniastme muutusest ja hapniku vakantside moodustumisest.

Termogravimeetrilise ja elektrokeemilise analüüsi tulemustest on näha, et $(La_{0.6}Sr_{0.4})_{0.99}CoO_{3-\delta}$ B-asendi dopeeriminte Ti^{4+} katiooniga tõstab materjali stabiilsust. Selgus, et massi muutus termilise tsükili jooksul oli väiksem materjalidel, mille B-asendit oli Ti^{4+} katiooniga modifitseeritud. See on põhjustatud hapniku vakantside moodustumise madalamast intensiivsusest. Lennuaja sekundaarioonide massispektromeetria ja röntgenfotoelektronspektroskoopia tulemustest järeldub, et B-asendit Ti^{4+} katiooniga dopeerimine vähendab materjalides Sr segregeerumist elektroodi pinnale, millest tulenevalt suureneb stabiilsus H_2O ja CO_2 suhtes.

Elektrokeemilise impedantsspektroskoopia tulemustest järeldati, et hapnikelektroodi negatiivse potentsiaali vähendamine põhjustas kogu polarisatsioonilise takistuse mõningast suurenemist. Lisaks oli negatiivsel hapnikelektroodi potentsiaalil tugevam mõju polarisatsioonilise takistuse väärtusele just madalamal hapniku osarõhul, mida saab seletada madalama hapniku keemilise potentsiaaliga gaasifaasis.

Samuti uuriti elektrokeemilise impedantsspektroskoopiaga H_2O ja CO_2 mõju hapnikelektroodi materjali aktiivsusele. Tulemustest saab järeldada, et $La_{0.6}Sr_{0.4}CoO_{3-\delta}$, $(La_{0.6}Sr_{0.4})_{0.99}CoO_{3-\delta}$ ja $(La_{0.6}Sr_{0.4})_{1.01}CoO_{3-\delta}$ degradeerumine kiirenes H_2O lisamisel gaasisegusse, eelkõige polarisatsiooniliste takistuste väärtuste suurenemise tõttu. Nende materjalide puhul täheldatud degradatsioon ei olnud pöörduv. Kui gaasisegu muudeti tagasi puhta sünteetilise õhu peale, siis polarisatsiooniliste takistuste väärtused jätkasid kasvamist. Siiski täheldati, et väike defitsiit A-asendis $(La_{0.6}Sr_{0.4})_{0.99}CoO_{3-\delta}$ parandab perovskiitse materjali stabiilsust.

Fe katioonidega modifitseeritud $La_{0.6}Sr_{0.4}Co_{0.2}Fe_{0.8}O_{3-\delta}$ näitas teistsugust käitumist H_2O juuresolekul, kui eelpool toodud hapnikelektrood materjalid.

Kasutades gaasisegus uuesti sünteetilist õhku, siis polarisatsiooniline takistuse väärtus vähenes, mis viitab $La_{0.6}Sr_{0.4}Co_{0.2}Fe_{0.8}O_{3-\delta}$ pöörduvale degradatsioonile.

Niiskusel on teistsugune mõju Ti^{4+} katioonidega dopeeritud $(La_{0.6}Sr_{0.4})_{0.99}Co_{1-x}Ti_xO_{3-\delta}$ materjalidele. Niiskuse lisand gaasisegus küll kiirendas $(La_{0.6}Sr_{0.4})_{0.99}Co_{0.98}Ti_{0.02}O_{3-\delta}$, $(La_{0.6}Sr_{0.4})_{0.99}Co_{0.96}Ti_{0.04}O_{3-\delta}$ ja $(La_{0.6}Sr_{0.4})_{0.99}Co_{0.94}Ti_{0.06}O_{3-\delta}$ materjalide degradatsiooni, kuid selle eemaldamisel degredeerumine peatus.

Materjalidel, millel on suurem kontsentratsioon Ti^{4+} B-asendis, nagu $(La_{0.6}Sr_{0.4})_{0.99}Co_{0.92}Ti_{0.08}O_{3-\delta}$ ja $(La_{0.6}Sr_{0.4})_{0.99}Co_{0.90}Ti_{0.10}O_{3-\delta}$ käitusid sarnaselt niiskuse juuresolekul nagu $La_{0.6}Sr_{0.4}CoO_{3-\delta}$, $(La_{0.6}Sr_{0.4})_{0.99}CoO_{3-\delta}$ ja $(La_{0.6}Sr_{0.4})_{1.01}CoO_{3-\delta}$.

CO_2 lisand sünteetilises õhus mõjutas $(La_{0.6}Sr_{0.4})_{0.99}CoO_{3-\delta}$ materjali stabiilsust samuti negatiivselt, tõstes degradeerumise kiirust. Lisaks oli protsess mittepöörduv, mis tähendab, et lisandi eemaldamisel degradeerumine jätkus. Tuleks rõhutada, et kõikide Ti^{4+} katioonidega modifitseeritud materjalide korral täheldati paranenud stabiilsust. $(La_{0.6}Sr_{0.4})_{0.99}Co_{0.98}Ti_{0.02}O_{3-\delta}$ ja $(La_{0.6}Sr_{0.4})_{0.99}Co_{0.96}Ti_{0.04}O_{3-\delta}$ materjalidel kiirendas CO_2 lisand degradeerumist kuid polarisatsioonilise takistuse väärtus vähenes lisandi eemaldamisel tagasi algse väärtuseni, kinnitades paranenud stabiilsust ja täielikult pöörduvat degradatsiooni. Osaliselt pöörduvat degradatsiooni täheldati $(La_{0.6}Sr_{0.4})_{0.99}Co_{0.94}Ti_{0.06}O_{3-\delta}$ ja $(La_{0.6}Sr_{0.4})_{0.99}Co_{0.92}Ti_{0.08}O_{3-\delta}$ korral. $(La_{0.6}Sr_{0.4})_{0.99}Co_{0.90}Ti_{0.10}O_{3-\delta}$ korral CO_2 kiirendas degradeerumist, mis aga lõppes lisandi eemaldamisel gaasisegust.

Kokkuvõtteks saab järeldada, et Ti^{4+} katioonidega modifitseeritud perovskiitsed hapnikelektroodi materjalid võimaldavad tõsta antud tehnoloogia töökindlust ja seejuures vähendada kulutusi gaaside puhastamise seadmetele.

10. ACKNOWLEDGMENTS

First of all, I would like to sincerely thank my supervisors, Indrek Kivi and professor Enn Lust. Thank you for always supporting me, expanding my worldview, and directing me to look at problems from a different angle. Enn, you are incredibly hardworking, which inspired me to work harder. Indrek, you are very supportive. If things are not going according to plan, you can always motivate me to find a solution. Indrek, also, thanks for my first discs – it has become a disease.

I would also like to thank Mr. Jaan Aruväli for XRD measurements and analyzes; Dr. Priit Möller for TOF-SIMS measurements; Dr. Kuno Kooser for XPS measurements and interpretation.

In addition, all the people in the chair of physical chemistry, thank you for the company and the supportive environment. Martin Maide, thank you for everything. I guess there is not a topic we have not discussed during all these years. I would like to thank Ove Korjus, Meelis Härmas, Riinu Härmas and Ronald Väli for moments spent together. I would also like to thank Dr. Thomas Thomberg and Dr. Heili Kasuk for their contribution to my progress inside and outside of the Chemicum.

Finally, I would like to highlight my family. Thank you for always being there. I would not be here without you, Mom, Dad. Thank you, Eva-Liisa, for supporting and loving me throughout this time. Thank you, sister and your family for being there and supporting me all these years.

This work was supported by the EU through the European Regional Development Fund under project TK141 “Advanced materials and high-technology devices for energy recuperation systems” (2014-2020.4.01.15-0011), Graduate School of Functional materials and technologies in University of Tartu, Higher education specialization stipends in smart specialization growth areas 2014-2020.4.02.16-0026, by the Estonian Research Council grant PRG 551, by the Estonian Research Council PUT1581 and by the Estonian Research Council (institutional research grant No. IUT20-13), Estonian Science Foundation ETF grant no. 7791 and 9352, the Estonian Centre of Excellence in Science Project TK 117T, the Estonian Energy Technology Progam project SLOKT10209T, European Spallation Source: Estonian Partition in ESS Instrument design, development and building, and application for scientific research SLOKT12026T and Estonian Energy Technology Program Project 3.2.0501.10–0015.

PUBLICATIONS

CURRICULUM VITAE

Name: Alar Heinsaar
Date of birth: February 22, 1992
Citizenship: Estonian
Contact: Institute of Chemistry, University of Tartu
Ravila 14a, 50411, Tartu, Estonia
E-mail: alar.heinsaar@ut.ee

Education:

2018–…	University of Tartu, Institute of Chemistry, PhD student
2013–2015	University of Tartu – Master's degree in chemistry
2010–2013	University of Tartu – Bachelor's degree in chemistry

Professional Employment:

2018–…	University of Tartu, Institute of Chemistry, Chemist
2012–2015	University of Tartu, Institute of Chemistry, Chemist

List of publications:

1. E. Lust, G. Nurk, P. Möller, I. Kivi, R. Kanarbik, K, Tamm, A. Heinsaar, Development of Medium-Temperature Solid Oxide Fuel Cell Materials and Single Cells in Estonia Cell Design, ECS Transactions 57 (1) (2013) 521–527.
2. I. Kivi, J. Aruväli, K. Kirsimäe, A. Heinsaar, G. Nurk, E. Lust, Oxygen stoichiometry in $La_{0.6}Sr_{0.4}CoO_{3-\delta}$ and $La_{0.6}Sr_{0.4}Co_{0.2}Fe_{0.8}O_{3-\delta}$ cathodes under applied potential as a function of temperature and oxygen partial pressure, measured by novel electrochemical in situ high-temperature XRD method, Journal of the Electrochemical Society 160 (9) (2013) F1022– F1026.
3. E. Lust, K. Tamm. G. Nurk, P. Möller, I. Kivi, R. Kanarbik, A. Heinsaar, Development of Medium-Temperature Solid Oxide Fuel Cells and CO_2 and H_2O Co-Electrolysis Cells in Estonia, ECS Transactions 68 (1) (2015) 3407–3415.
4. I. Kivi, J. Aruväli, K. Kirsimäe, A. Heinsaar, G. Nurk, E. Lust, Changes in SOFC Cathode Crystallographic Structure Induced by Temperature, Potential and Oxygen Partial Pressure Studied Using in-situ HT-XRD, ECS Transactions 68 (1) (2015) 671–679.
5. I. Kivi, J. Aruväli, K. Kirsimäe, A. Heinsaar, G. Nurk, E. Lust, Kinetic response of $La_{0.6}Sr_{0.4}CoO_{3-\delta}$ lattice parameters to electric potential change in porous cathode at in situ solid oxide fuel cell conditions, Journal of the Electrochemical Society 162 (3) (2015) F354–F358.
6. I. Kivi, J. Aruväli, K. Kirsimäe, P. Möller, A. Heinsaar, G. Nurk, E. Lust, Influence of humidified synthetic air feeding conditions on the stoichiometry of $(La_{1-x}Sr_x)_yCoO_{3-\delta}$ and $La_{0.6}Sr_{0.4}Co_{0.2}Fe_{0.8}O_{3-\delta}$ cathodes under applied

potential measured by electrochemical in situ high-temperature XRD method, Journal of the Electrochemical Society 21 (2) (2017) 361− 369.
7. A. Heinsaar, I. Kivi, G. Nurk, J. Aruväli, E. Lust, Influence of Humidity and Carbon Dioxide on the $(La_{0.6}Sr_{0.4})_{0.99}Co_{1-x}M_xO_{3-\delta}$ (M = Nb, Ti) Oxygen Electrode Characteristics, ECS Transactions 91 (1) (2019) 1453−1460.
8. A. Heinsaar, I. Kivi, P. Möller, K. Kooser, T. Käämbre, J. Aruväli, E. Lust, G. Nurk, Influence of the Ti content on the electrochemical performance and surface properties of $(La_{0.6}Sr_{0.4})_{0.99}Co_{1-x}Ti_xO_{3-\delta}$ oxygen electrode, ECS Transactions 103 (1) (2021) 1433−1444.
9. A. Heinsaar, I. Kivi, P. Möller, K. Kooser, T. Käämbre, J. Aruväli, G. Nurk, E. Lust, Influence of Carbon Dioxide and Humidity on the Stability of $(La_{0.6}Sr_{0.4})_{0.99}Co_{1-x}Ti_xO_{3-\delta}$ Cathode, Journal of the Electrochemical Society 169 (1) (2022) 014514.

ELULOOKIRJELDUS

Nimi: Alar Heinsaar
Sünniaeg: 22. veebruar 1992
Kodakondsus: Eesti
Aadress: Keemia instituut, Tartu Ülikool
Ravila 14a, 50411, Tartu, Eesti
E-post: alar.heinsaar@ut.ee

Haridustee:

2018–…	Tartu Ülikool, Keemia instituut, doktorant
2013–2015	Tartu Ülikool – Magistrikraad keemias
2010–2013	Tartu Ülikool – Bakalaureusekraad keemias

Teenistuskäik:

2018–…	Tartu Ülikool, Keemia instituut, keemik
2012–2015	Tartu Ülikool, Keemia instituut, keemik

Teaduspublikatsioonid:

1. E. Lust, G. Nurk, P. Möller, I. Kivi, R. Kanarbik, K, Tamm, A. Heinsaar, Development of Medium-Temperature Solid Oxide Fuel Cell Materials and Single Cells in Estonia Cell Design, ECS Transactions 57 (1) (2013) 521−527.
2. I. Kivi, J. Aruväli, K. Kirsimäe, A. Heinsaar, G. Nurk, E. Lust, Oxygen stoichiometry in $La_{0.6}Sr_{0.4}CoO_{3-\delta}$ and $La_{0.6}Sr_{0.4}Co_{0.2}Fe_{0.8}O_{3-\delta}$ cathodes under applied potential as a function of temperature and oxygen partial pressure, measured by novel electrochemical in situ high-temperature XRD method, Journal of the Electrochemical Society 160 (9) (2013) F1022− F1026.
3. E. Lust, K. Tamm. G. Nurk, P. Möller, I. Kivi, R. Kanarbik, A. Heinsaar, Development of Medium-Temperature Solid Oxide Fuel Cells and CO_2 and H_2O Co-Electrolysis Cells in Estonia, ECS Transactions 68 (1) (2015) 3407−3415.
4. I. Kivi, J. Aruväli, K. Kirsimäe, A. Heinsaar, G. Nurk, E. Lust, Changes in SOFC Cathode Crystallographic Structure Induced by Temperature, Potential and Oxygen Partial Pressure Studied Using in-situ HT-XRD, ECS Transactions 68 (1) (2015) 671−679.
5. I. Kivi, J. Aruväli, K. Kirsimäe, A. Heinsaar, G. Nurk, E. Lust, Kinetic response of $La_{0.6}Sr_{0.4}CoO_{3-\delta}$ lattice parameters to electric potential change in porous cathode at in situ solid oxide fuel cell conditions, Journal of the Electrochemical Society 162 (3) (2015) F354−F358.
6. I. Kivi, J. Aruväli, K. Kirsimäe, P. Möller, A. Heinsaar, G. Nurk, E. Lust, Influence of humidified synthetic air feeding conditions on the stoichiometry of $(La_{1-x}Sr_x)_yCoO_{3-\delta}$ and $La_{0.6}Sr_{0.4}Co_{0.2}Fe_{0.8}O_{3-\delta}$ cathodes under applied

potential measured by electrochemical in situ high-temperature XRD method, Journal of the Electrochemical Society 21 (2) (2017) 361−369.
7. A. Heinsaar, I. Kivi, G. Nurk, J. Aruväli, E. Lust, Influence of Humidity and Carbon Dioxide on the $(La_{0.6}Sr_{0.4})_{0.99}Co_{1-x}M_xO_{3-\delta}$ (M = Nb, Ti) Oxygen Electrode Characteristics, ECS Transactions 91 (1) (2019) 1453−1460.
8. A. Heinsaar, I. Kivi, P. Möller, K. Kooser, T. Käämbre, J. Aruväli, E. Lust, G. Nurk, Influence of the Ti content on the electrochemical performance and surface properties of $(La_{0.6}Sr_{0.4})_{0.99}Co_{1-x}Ti_xO_{3-\delta}$ oxygen electrode, ECS Transactions 103 (1) (2021) 1433−1444.
9. A. Heinsaar, I. Kivi, P. Möller, K. Kooser, T. Käämbre, J. Aruväli, G. Nurk, E. Lust, Influence of Carbon Dioxide and Humidity on the Stability of $(La_{0.6}Sr_{0.4})_{0.99}Co_{1-x}Ti_xO_{3-\delta}$ Cathode, Journal of the Electrochemical Society 169 (1) (2022) 014514.

DISSERTATIONES CHIMICAE UNIVERSITATIS TARTUENSIS

1. **Toomas Tamm.** Quantum-chemical simulation of solvent effects. Tartu, 1993, 110 p.
2. **Peeter Burk.** Theoretical study of gas-phase acid-base equilibria. Tartu, 1994, 96 p.
3. **Victor Lobanov.** Quantitative structure-property relationships in large descriptor spaces. Tartu, 1995, 135 p.
4. **Vahur Mäemets.** The ^{17}O and ^{1}H nuclear magnetic resonance study of H_2O in individual solvents and its charged clusters in aqueous solutions of electrolytes. Tartu, 1997, 140 p.
5. **Andrus Metsala.** Microcanonical rate constant in nonequilibrium distribution of vibrational energy and in restricted intramolecular vibrational energy redistribution on the basis of slater's theory of unimolecular reactions. Tartu, 1997, 150 p.
6. **Uko Maran.** Quantum-mechanical study of potential energy surfaces in different environments. Tartu, 1997, 137 p.
7. **Alar Jänes.** Adsorption of organic compounds on antimony, bismuth and cadmium electrodes. Tartu, 1998, 219 p.
8. **Kaido Tammeveski.** Oxygen electroreduction on thin platinum films and the electrochemical detection of superoxide anion. Tartu, 1998, 139 p.
9. **Ivo Leito.** Studies of Brønsted acid-base equilibria in water and non-aqueous media. Tartu, 1998, 101 p.
10. **Jaan Leis.** Conformational dynamics and equilibria in amides. Tartu, 1998, 131 p.
11. **Toonika Rinken.** The modelling of amperometric biosensors based on oxidoreductases. Tartu, 2000, 108 p.
12. **Dmitri Panov.** Partially solvated Grignard reagents. Tartu, 2000, 64 p.
13. **Kaja Orupõld.** Treatment and analysis of phenolic wastewater with microorganisms. Tartu, 2000, 123 p.
14. **Jüri Ivask.** Ion Chromatographic determination of major anions and cations in polar ice core. Tartu, 2000, 85 p.
15. **Lauri Vares.** Stereoselective Synthesis of Tetrahydrofuran and Tetrahydropyran Derivatives by Use of Asymmetric Horner-Wadsworth-Emmons and Ring Closure Reactions. Tartu, 2000, 184 p.
16. **Martin Lepiku.** Kinetic aspects of dopamine D_2 receptor interactions with specific ligands. Tartu, 2000, 81 p.
17. **Katrin Sak.** Some aspects of ligand specificity of P2Y receptors. Tartu, 2000, 106 p.
18. **Vello Pällin.** The role of solvation in the formation of iotsitch complexes. Tartu, 2001, 95 p.
19. **Katrin Kollist.** Interactions between polycyclic aromatic compounds and humic substances. Tartu, 2001, 93 p.

20. **Ivar Koppel.** Quantum chemical study of acidity of strong and superstrong Brønsted acids. Tartu, 2001, 104 p.
21. **Viljar Pihl.** The study of the substituent and solvent effects on the acidity of OH and CH acids. Tartu, 2001, 132 p.
22. **Natalia Palm.** Specification of the minimum, sufficient and significant set of descriptors for general description of solvent effects. Tartu, 2001, 134 p.
23. **Sulev Sild.** QSPR/QSAR approaches for complex molecular systems. Tartu, 2001, 134 p.
24. **Ruslan Petrukhin.** Industrial applications of the quantitative structure-property relationships. Tartu, 2001, 162 p.
25. **Boris V. Rogovoy.** Synthesis of (benzotriazolyl)carboximidamides and their application in relations with *N*- and *S*-nucleophyles. Tartu, 2002, 84 p.
26. **Koit Herodes.** Solvent effects on UV-vis absorption spectra of some solvatochromic substances in binary solvent mixtures: the preferential solvation model. Tartu, 2002, 102 p.
27. **Anti Perkson.** Synthesis and characterisation of nanostructured carbon. Tartu, 2002, 152 p.
28. **Ivari Kaljurand.** Self-consistent acidity scales of neutral and cationic Brønsted acids in acetonitrile and tetrahydrofuran. Tartu, 2003, 108 p.
29. **Karmen Lust.** Adsorption of anions on bismuth single crystal electrodes. Tartu, 2003, 128 p.
30. **Mare Piirsalu.** Substituent, temperature and solvent effects on the alkaline hydrolysis of substituted phenyl and alkyl esters of benzoic acid. Tartu, 2003, 156 p.
31. **Meeri Sassian.** Reactions of partially solvated Grignard reagents. Tartu, 2003, 78 p.
32. **Tarmo Tamm.** Quantum chemical modelling of polypyrrole. Tartu, 2003. 100 p.
33. **Erik Teinemaa.** The environmental fate of the particulate matter and organic pollutants from an oil shale power plant. Tartu, 2003. 102 p.
34. **Jaana Tammiku-Taul.** Quantum chemical study of the properties of Grignard reagents. Tartu, 2003. 120 p.
35. **Andre Lomaka.** Biomedical applications of predictive computational chemistry. Tartu, 2003. 132 p.
36. **Kostyantyn Kirichenko.** Benzotriazole – Mediated Carbon–Carbon Bond Formation. Tartu, 2003. 132 p.
37. **Gunnar Nurk.** Adsorption kinetics of some organic compounds on bismuth single crystal electrodes. Tartu, 2003, 170 p.
38. **Mati Arulepp.** Electrochemical characteristics of porous carbon materials and electrical double layer capacitors. Tartu, 2003, 196 p.
39. **Dan Cornel Fara.** QSPR modeling of complexation and distribution of organic compounds. Tartu, 2004, 126 p.
40. **Riina Mahlapuu.** Signalling of galanin and amyloid precursor protein through adenylate cyclase. Tartu, 2004, 124 p.

41. **Mihkel Kerikmäe.** Some luminescent materials for dosimetric applications and physical research. Tartu, 2004, 143 p.
42. **Jaanus Kruusma.** Determination of some important trace metal ions in human blood. Tartu, 2004, 115 p.
43. **Urmas Johanson.** Investigations of the electrochemical properties of polypyrrole modified electrodes. Tartu, 2004, 91 p.
44. **Kaido Sillar.** Computational study of the acid sites in zeolite ZSM-5. Tartu, 2004, 80 p.
45. **Aldo Oras.** Kinetic aspects of dATPαS interaction with $P2Y_1$ receptor. Tartu, 2004, 75 p.
46. **Erik Mölder.** Measurement of the oxygen mass transfer through the air-water interface. Tartu, 2005, 73 p.
47. **Thomas Thomberg.** The kinetics of electroreduction of peroxodisulfate anion on cadmium (0001) single crystal electrode. Tartu, 2005, 95 p.
48. **Olavi Loog.** Aspects of condensations of carbonyl compounds and their imine analogues. Tartu, 2005, 83 p.
49. **Siim Salmar.** Effect of ultrasound on ester hydrolysis in aqueous ethanol. Tartu, 2006, 73 p.
50. **Ain Uustare.** Modulation of signal transduction of heptahelical receptors by other receptors and G proteins. Tartu, 2006, 121 p.
51. **Sergei Yurchenko.** Determination of some carcinogenic contaminants in food. Tartu, 2006, 143 p.
52. **Kaido Tämm.** QSPR modeling of some properties of organic compounds. Tartu, 2006, 67 p.
53. **Olga Tšubrik.** New methods in the synthesis of multisubstituted hydrazines. Tartu. 2006, 183 p.
54. **Lilli Sooväli.** Spectrophotometric measurements and their uncertainty in chemical analysis and dissociation constant measurements. Tartu, 2006, 125 p.
55. **Eve Koort.** Uncertainty estimation of potentiometrically measured ph and pK_a values. Tartu, 2006, 139 p.
56. **Sergei Kopanchuk.** Regulation of ligand binding to melanocortin receptor subtypes. Tartu, 2006, 119 p.
57. **Silvar Kallip.** Surface structure of some bismuth and antimony single crystal electrodes. Tartu, 2006, 107 p.
58. **Kristjan Saal.** Surface silanization and its application in biomolecule coupling. Tartu, 2006, 77 p.
59. **Tanel Tätte.** High viscosity $Sn(OBu)_4$ oligomeric concentrates and their applications in technology. Tartu, 2006, 91 p.
60. **Dimitar Atanasov Dobchev**. Robust QSAR methods for the prediction of properties from molecular structure. Tartu, 2006, 118 p.
61. **Hannes Hagu**. Impact of ultrasound on hydrophobic interactions in solutions. Tartu, 2007, 81 p.
62. **Rutha Jäger.** Electroreduction of peroxodisulfate anion on bismuth electrodes. Tartu, 2007, 142 p.

63. **Kaido Viht.** Immobilizable bisubstrate-analogue inhibitors of basophilic protein kinases: development and application in biosensors. Tartu, 2007, 88 p.
64. **Eva-Ingrid Rõõm.** Acid-base equilibria in nonpolar media. Tartu, 2007, 156 p.
65. **Sven Tamp.** DFT study of the cesium cation containing complexes relevant to the cesium cation binding by the humic acids. Tartu, 2007, 102 p.
66. **Jaak Nerut.** Electroreduction of hexacyanoferrate(III) anion on Cadmium (0001) single crystal electrode. Tartu, 2007, 180 p.
67. **Lauri Jalukse.** Measurement uncertainty estimation in amperometric dissolved oxygen concentration measurement. Tartu, 2007, 112 p.
68. **Aime Lust.** Charge state of dopants and ordered clusters formation in CaF_2:Mn and CaF_2:Eu luminophors. Tartu, 2007, 100 p.
69. **Iiris Kahn**. Quantitative Structure-Activity Relationships of environmentally relevant properties. Tartu, 2007, 98 p.
70. **Mari Reinik.** Nitrates, nitrites, N-nitrosamines and polycyclic aromatic hydrocarbons in food: analytical methods, occurrence and dietary intake. Tartu, 2007, 172 p.
71. **Heili Kasuk.** Thermodynamic parameters and adsorption kinetics of organic compounds forming the compact adsorption layer at Bi single crystal electrodes. Tartu, 2007, 212 p.
72. **Erki Enkvist.** Synthesis of adenosine-peptide conjugates for biological applications. Tartu, 2007, 114 p.
73. **Svetoslav Hristov Slavov**. Biomedical applications of the QSAR approach. Tartu, 2007, 146 p.
74. **Eneli Härk.** Electroreduction of complex cations on electrochemically polished Bi(*hkl*) single crystal electrodes. Tartu, 2008, 158 p.
75. **Priit Möller.** Electrochemical characteristics of some cathodes for medium temperature solid oxide fuel cells, synthesized by solid state reaction technique. Tartu, 2008, 90 p.
76. **Signe Viggor.** Impact of biochemical parameters of genetically different pseudomonads at the degradation of phenolic compounds. Tartu, 2008, 122 p.
77. **Ave Sarapuu.** Electrochemical reduction of oxygen on quinone-modified carbon electrodes and on thin films of platinum and gold. Tartu, 2008, 134 p.
78. **Agnes Kütt.** Studies of acid-base equilibria in non-aqueous media. Tartu, 2008, 198 p.
79. **Rouvim Kadis.** Evaluation of measurement uncertainty in analytical chemistry: related concepts and some points of misinterpretation. Tartu, 2008, 118 p.
80. **Valter Reedo.** Elaboration of IVB group metal oxide structures and their possible applications. Tartu, 2008, 98 p.
81. **Aleksei Kuznetsov.** Allosteric effects in reactions catalyzed by the cAMP-dependent protein kinase catalytic subunit. Tartu, 2009, 133 p.

82. **Aleksei Bredihhin.** Use of mono- and polyanions in the synthesis of multisubstituted hydrazine derivatives. Tartu, 2009, 105 p.
83. **Anu Ploom.** Quantitative structure-reactivity analysis in organosilicon chemistry. Tartu, 2009, 99 p.
84. **Argo Vonk.** Determination of adenosine A_{2A}- and dopamine D_1 receptor-specific modulation of adenylate cyclase activity in rat striatum. Tartu, 2009, 129 p.
85. **Indrek Kivi.** Synthesis and electrochemical characterization of porous cathode materials for intermediate temperature solid oxide fuel cells. Tartu, 2009, 177 p.
86. **Jaanus Eskusson.** Synthesis and characterisation of diamond-like carbon thin films prepared by pulsed laser deposition method. Tartu, 2009, 117 p.
87. **Marko Lätt.** Carbide derived microporous carbon and electrical double layer capacitors. Tartu, 2009, 107 p.
88. **Vladimir Stepanov.** Slow conformational changes in dopamine transporter interaction with its ligands. Tartu, 2009, 103 p.
89. **Aleksander Trummal.** Computational Study of Structural and Solvent Effects on Acidities of Some Brønsted Acids. Tartu, 2009, 103 p.
90. **Eerold Vellemäe.** Applications of mischmetal in organic synthesis. Tartu, 2009, 93 p.
91. **Sven Parkel.** Ligand binding to 5-HT_{1A} receptors and its regulation by Mg^{2+} and Mn^{2+}. Tartu, 2010, 99 p.
92. **Signe Vahur.** Expanding the possibilities of ATR-FT-IR spectroscopy in determination of inorganic pigments. Tartu, 2010, 184 p.
93. **Tavo Romann**. Preparation and surface modification of bismuth thin film, porous, and microelectrodes. Tartu, 2010, 155 p.
94. **Nadežda Aleksejeva.** Electrocatalytic reduction of oxygen on carbon nanotube-based nanocomposite materials. Tartu, 2010, 147 p.
95. **Marko Kullapere.** Electrochemical properties of glassy carbon, nickel and gold electrodes modified with aryl groups. Tartu, 2010, 233 p.
96. **Liis Siinor.** Adsorption kinetics of ions at Bi single crystal planes from aqueous electrolyte solutions and room-temperature ionic liquids. Tartu, 2010, 101 p.
97. **Angela Vaasa.** Development of fluorescence-based kinetic and binding assays for characterization of protein kinases and their inhibitors. Tartu 2010, 101 p.
98. **Indrek Tulp.** Multivariate analysis of chemical and biological properties. Tartu 2010, 105 p.
99. **Aare Selberg.** Evaluation of environmental quality in Northern Estonia by the analysis of leachate. Tartu 2010, 117 p.
100. **Darja Lavõgina.** Development of protein kinase inhibitors based on adenosine analogue-oligoarginine conjugates. Tartu 2010, 248 p.
101. **Laura Herm.** Biochemistry of dopamine D_2 receptors and its association with motivated behaviour. Tartu 2010, 156 p.

102. **Terje Raudsepp.** Influence of dopant anions on the electrochemical properties of polypyrrole films. Tartu 2010, 112 p.
103. **Margus Marandi.** Electroformation of Polypyrrole Films: *In-situ* AFM and STM Study. Tartu 2011, 116 p.
104. **Kairi Kivirand.** Diamine oxidase-based biosensors: construction and working principles. Tartu, 2011, 140 p.
105. **Anneli Kruve.** Matrix effects in liquid-chromatography electrospray mass-spectrometry. Tartu, 2011, 156 p.
106. **Gary Urb.** Assessment of environmental impact of oil shale fly ash from PF and CFB combustion. Tartu, 2011, 108 p.
107. **Nikita Oskolkov.** A novel strategy for peptide-mediated cellular delivery and induction of endosomal escape. Tartu, 2011, 106 p.
108. **Dana Martin.** The QSPR/QSAR approach for the prediction of properties of fullerene derivatives. Tartu, 2011, 98 p.
109. **Säde Viirlaid.** Novel glutathione analogues and their antioxidant activity. Tartu, 2011, 106 p.
110. **Ülis Sõukand.** Simultaneous adsorption of Cd^{2+}, Ni^{2+}, and Pb^{2+} on peat. Tartu, 2011, 124 p.
111. **Lauri Lipping.** The acidity of strong and superstrong Brønsted acids, an outreach for the "limits of growth": a quantum chemical study. Tartu, 2011, 124 p.
112. **Heisi Kurig.** Electrical double-layer capacitors based on ionic liquids as electrolytes. Tartu, 2011, 146 p.
113. **Marje Kasari.** Bisubstrate luminescent probes, optical sensors and affinity adsorbents for measurement of active protein kinases in biological samples. Tartu, 2012, 126 p.
114. **Kalev Takkis.** Virtual screening of chemical databases for bioactive molecules. Tartu, 2012, 122 p.
115. **Ksenija Kisseljova**. Synthesis of aza-β^3-amino acid containing peptides and kinetic study of their phosphorylation by protein kinase A. Tartu, 2012, 104 p.
116. **Riin Rebane.** Advanced method development strategy for derivatization LC/ESI/MS. Tartu, 2012, 184 p.
117. **Vladislav Ivaništšev.** Double layer structure and adsorption kinetics of ions at metal electrodes in room temperature ionic liquids. Tartu, 2012, 128 p.
118. **Irja Helm.** High accuracy gravimetric Winkler method for determination of dissolved oxygen. Tartu, 2012, 139 p.
119. **Karin Kipper.** Fluoroalcohols as Components of LC-ESI-MS Eluents: Usage and Applications. Tartu, 2012, 164 p.
120. **Arno Ratas.** Energy storage and transfer in dosimetric luminescent materials. Tartu, 2012, 163 p.
121. **Reet Reinart-Okugbeni**. Assay systems for characterisation of subtype-selective binding and functional activity of ligands on dopamine receptors. Tartu, 2012, 159 p.

122. **Lauri Sikk.** Computational study of the Sonogashira cross-coupling reaction. Tartu, 2012, 81 p.
123. **Karita Raudkivi.** Neurochemical studies on inter-individual differences in affect-related behaviour of the laboratory rat. Tartu, 2012, 161 p.
124. **Indrek Saar.** Design of GalR2 subtype specific ligands: their role in depression-like behavior and feeding regulation. Tartu, 2013, 126 p.
125. **Ann Laheäär.** Electrochemical characterization of alkali metal salt based non-aqueous electrolytes for supercapacitors. Tartu, 2013, 127 p.
126. **Kerli Tõnurist.** Influence of electrospun separator materials properties on electrochemical performance of electrical double-layer capacitors. Tartu, 2013, 147 p.
127. **Kaija Põhako-Esko.** Novel organic and inorganic ionogels: preparation and characterization. Tartu, 2013, 124 p.
128. **Ivar Kruusenberg.** Electroreduction of oxygen on carbon nanomaterial-based catalysts. Tartu, 2013, 191 p.
129. **Sander Piiskop.** Kinetic effects of ultrasound in aqueous acetonitrile solutions. Tartu, 2013, 95 p.
130. **Ilona Faustova**. Regulatory role of L-type pyruvate kinase N-terminal domain. Tartu, 2013, 109 p.
131. **Kadi Tamm.** Synthesis and characterization of the micro-mesoporous anode materials and testing of the medium temperature solid oxide fuel cell single cells. Tartu, 2013, 138 p.
132. **Iva Bozhidarova Stoyanova-Slavova.** Validation of QSAR/QSPR for regulatory purposes. Tartu, 2013, 109 p.
133. **Vitali Grozovski**. Adsorption of organic molecules at single crystal electrodes studied by *in situ* STM method. Tartu, 2014, 146 p.
134. **Santa Veikšina**. Development of assay systems for characterisation of ligand binding properties to melanocortin 4 receptors. Tartu, 2014, 151 p.
135. **Jüri Liiv.** PVDF (polyvinylidene difluoride) as material for active element of twisting-ball displays. Tartu, 2014, 111 p.
136. **Kersti Vaarmets.** Electrochemical and physical characterization of pristine and activated molybdenum carbide-derived carbon electrodes for the oxygen electroreduction reaction. Tartu, 2014, 131 p.
137. **Lauri Tõntson**. Regulation of G-protein subtypes by receptors, guanine nucleotides and Mn^{2+}. Tartu, 2014, 105 p.
138. **Aiko Adamson.** Properties of amine-boranes and phosphorus analogues in the gas phase. Tartu, 2014, 78 p.
139. **Elo Kibena**. Electrochemical grafting of glassy carbon, gold, highly oriented pyrolytic graphite and chemical vapour deposition-grown graphene electrodes by diazonium reduction method. Tartu, 2014, 184 p.
140. **Teemu Näykki.** Novel Tools for Water Quality Monitoring – From Field to Laboratory. Tartu, 2014, 202 p.
141. **Karl Kaupmees.** Acidity and basicity in non-aqueous media: importance of solvent properties and purity. Tartu, 2014, 128 p.

142. **Oleg Lebedev**. Hydrazine polyanions: different strategies in the synthesis of heterocycles. Tartu, 2015, 118 p.
143. **Geven Piir.** Environmental risk assessment of chemicals using QSAR methods. Tartu, 2015, 123 p.
144. **Olga Mazina.** Development and application of the biosensor assay for measurements of cyclic adenosine monophosphate in studies of G protein-coupled receptor signalinga. Tartu, 2015, 116 p.
145. **Sandip Ashokrao Kadam.** Anion receptors: synthesis and accurate binding measurements. Tartu, 2015, 116 p.
146. **Indrek Tallo.** Synthesis and characterization of new micro-mesoporous carbide derived carbon materials for high energy and power density electrical double layer capacitors. Tartu, 2015, 148 p.
147. **Heiki Erikson.** Electrochemical reduction of oxygen on nanostructured palladium and gold catalysts. Tartu, 2015, 204 p.
148. **Erik Anderson.** *In situ* Scanning Tunnelling Microscopy studies of the interfacial structure between Bi(111) electrode and a room temperature ionic liquid. Tartu, 2015, 118 p.
149. **Girinath G. Pillai.** Computational Modelling of Diverse Chemical, Biochemical and Biomedical Properties. Tartu, 2015, 140 p.
150. **Piret Pikma.** Interfacial structure and adsorption of organic compounds at Cd(0001) and Sb(111) electrodes from ionic liquid and aqueous electrolytes: an *in situ* STM study. Tartu, 2015, 126 p.
151. **Ganesh babu Manoharan.** Combining chemical and genetic approaches for photoluminescence assays of protein kinases. Tartu, 2016, 126 p.
152. **Carolin Siimenson**. Electrochemical characterization of halide ion adsorption from liquid mixtures at Bi(111) and pyrolytic graphite electrode surface. Tartu, 2016, 110 p.
153. **Asko Laaniste.** Comparison and optimisation of novel mass spectrometry ionisation sources. Tartu, 2016, 156 p.
154. **Hanno Evard.** Estimating limit of detection for mass spectrometric analysis methods. Tartu, 2016, 224 p.
155. **Kadri Ligi.** Characterization and application of protein kinase-responsive organic probes with triplet-singlet energy transfer. Tartu, 2016, 122 p.
156. **Margarita Kagan.** Biosensing penicillins' residues in milk flows. Tartu, 2016, 130 p.
157. **Marie Kriisa.** Development of protein kinase-responsive photoluminescent probes and cellular regulators of protein phosphorylation. Tartu, 2016, 106 p.
158. **Mihkel Vestli.** Ultrasonic spray pyrolysis deposited electrolyte layers for intermediate temperature solid oxide fuel cells. Tartu, 2016, 156 p.
159. **Silver Sepp**. Influence of porosity of the carbide-derived carbon on the properties of the composite electrocatalysts and characteristics of polymer electrolyte fuel cells. Tartu, 2016, 137 p.
160. **Kristjan Haav**. Quantitative relative equilibrium constant measurements in supramolecular chemistry. Tartu, 2017, 158 p.

161. **Anu Teearu**. Development of MALDI-FT-ICR-MS methodology for the analysis of resinous materials. Tartu, 2017, 205 p.
162. **Taavi Ivan**. Bifunctional inhibitors and photoluminescent probes for studies on protein complexes. Tartu, 2017, 140 p.
163. **Maarja-Liisa Oldekop**. Characterization of amino acid derivatization reagents for LC-MS analysis. Tartu, 2017, 147 p.
164. **Kristel Jukk**. Electrochemical reduction of oxygen on platinum- and palladium-based nanocatalysts. Tartu, 2017, 250 p.
165. **Siim Kukk**. Kinetic aspects of interaction between dopamine transporter and *N*-substituted nortropane derivatives. Tartu, 2017, 107 p.
166. **Birgit Viira**. Design and modelling in early drug development in targeting HIV-1 reverse transcriptase and Malaria. Tartu, 2017, 172 p.
167. **Rait Kivi**. Allostery in cAMP dependent protein kinase catalytic subunit. Tartu, 2017, 115 p.
168. **Agnes Heering**. Experimental realization and applications of the unified acidity scale. Tartu, 2017, 123 p.
169. **Delia Juronen**. Biosensing system for the rapid multiplex detection of mastitis-causing pathogens in milk. Tartu, 2018, 85 p.
170. **Hedi Rahnel.** ARC-inhibitors: from reliable biochemical assays to regulators of physiology of cells. Tartu, 2018, 176 p.
171. **Anton Ruzanov.** Computational investigation of the electrical double layer at metal–aqueous solution and metal–ionic liquid interfaces. Tartu, 2018, 129 p.
172. **Katrin Kestav.** Crystal Structure-Guided Development of Bisubstrate-Analogue Inhibitors of Mitotic Protein Kinase Haspin. Tartu, 2018, 166 p.
173. **Mihkel Ilisson.** Synthesis of novel heterocyclic hydrazine derivatives and their conjugates. Tartu, 2018, 101 p.
174. **Anni Allikalt.** Development of assay systems for studying ligand binding to dopamine receptors. Tartu, 2018, 160 p.
175. **Ove Oll.** Electrical double layer structure and energy storage characteristics of ionic liquid based capacitors. Tartu, 2018, 187 p.
176. **Rasmus Palm.** Carbon materials for energy storage applications. Tartu, 2018, 114 p.
177. **Jörgen Metsik.** Preparation and stability of poly(3,4-ethylenedioxythiophene) thin films for transparent electrode applications. Tartu, 2018, 111 p.
178. **Sofja Tšepelevitš.** Experimental studies and modeling of solute-solvent interactions. Tartu, 2018, 109 p.
179. **Märt Lõkov.** Basicity of some nitrogen, phosphorus and carbon bases in acetonitrile. Tartu, 2018, 104 p.
180. **Anton Mastitski**. Preparation of α-aza-amino acid precursors and related compounds by novel methods of reductive one-pot alkylation and direct alkylation. Tartu, 2018, 155 p.
181. **Jürgen Vahter**. Development of bisubstrate inhibitors for protein kinase CK2. Tartu, 2019, 186 p.

182. **Piia Liigand.** Expanding and improving methodology and applications of ionization efficiency measurements. Tartu, 2019, 189 p.
183. **Sigrid Selberg.** Synthesis and properties of lipophilic phosphazene-based indicator molecules. Tartu, 2019, 74 p.
184. **Jaanus Liigand.** Standard substance free quantification for LC/ESI/MS analysis based on the predicted ionization efficiencies. Tartu, 2019, 254 p.
185. **Marek Mooste.** Surface and electrochemical characterisation of aryl film and nanocomposite material modified carbon and metal-based electrodes. Tartu, 2019, 304 p.
186. **Mare Oja.** Experimental investigation and modelling of pH profiles for effective membrane permeability of drug substances. Tartu, 2019, 306 p.
187. **Sajid Hussain.** Electrochemical reduction of oxygen on supported Pt catalysts. Tartu, 2019, 220 p.
188. **Ronald Väli.** Glucose-derived hard carbon electrode materials for sodium-ion batteries. Tartu, 2019, 180 p.
189. **Ester Tee.** Analysis and development of selective synthesis methods of hierarchical micro- and mesoporous carbons. Tartu, 2019, 210 p.
190. **Martin Maide.** Influence of the microstructure and chemical composition of the fuel electrode on the electrochemical performance of reversible solid oxide fuel cell. Tartu, 2020, 144 p.
191. **Edith Viirlaid.** Biosensing Pesticides in Water Samples. Tartu, 2020, 102 p.
192. **Maike Käärik.** Nanoporous carbon: the controlled nanostructure, and structure-property relationships. Tartu, 2020, 162 p.
193. **Artur Gornischeff.** Study of ionization efficiencies for derivatized compounds in LC/ESI/MS and their application for targeted analysis. Tartu, 2020, 124 p.
194. **Reet Link.** Ligand binding, allosteric modulation and constitutive activity of melanocortin-4 receptors. Tartu, 2020, 108 p.
195. **Pilleriin Peets.** Development of instrumental methods for the analysis of textile fibres and dyes. Tartu, 2020, 150 p.
196. **Larisa Ivanova.** Design of active compounds against neurodegenerative diseases. Tartu, 2020, 152 p.
197. **Meelis Härmas.** Impact of activated carbon microstructure and porosity on electrochemical performance of electrical double-layer capacitors. Tartu, 2020, 122 p.
198. **Ruta Hecht.** Novel Eluent Additives for LC-MS Based Bioanalytical Methods. Tartu, 2020, 202 p.
199. **Max Hecht.** Advances in the Development of a Point-of-Care Mass Spectrometer Test. Tartu, 2020, 168 p.
200. **Ida Rahu.** Bromine formation in inorganic bromide/nitrate mixtures and its application for oxidative aromatic bromination. Tartu, 2020, 116 p.
201. **Sander Ratso**. Electrocatalysis of oxygen reduction on non-precious metal catalysts. Tartu, 2020, 371 p.
202. **Astrid Darnell.** Computational design of anion receptors and evaluation of host-guest binding. Tartu, 2021, 150 p.

203. **Ove Korjus.** The development of ceramic fuel electrode for solid oxide cells. Tartu, 2021, 150 p.
204. **Merit Oss.** Ionization efficiency in electrospray ionization source and its relations to compounds' physico-chemical properties. Tartu, 2021, 124 p.
205. **Madis Lüsi**. Electroreduction of oxygen on nanostructured palladium catalysts. Tartu, 2021, 180 p.
206. **Eliise Tammekivi.** Derivatization and quantitative gas-chromatographic analysis of oils. Tartu, 2021, 122 p.
207. **Simona Selberg.** Development of Small-Molecule Regulators of Epi-transcriptomic Processes. Tartu, 2021, 122 p.
208. **Olivier Etebe Nonga.** Inhibitors and photoluminescent probes for in vitro studies on protein kinases PKA and PIM. Tartu, 2021, 189 p.
209. **Riinu Härmas.** The structure and H2 diffusion in porous carbide-derived carbon particles. Tartu, 2022, 123 p.
210. **Maarja Paalo.** Synthesis and characterization of novel carbon electrodes for high power density electrochemical capacitors. Tartu, 2022, 144 p.
211. **Jinfeng Zhao.** Electrochemical characteristics of Bi(hkl) and micro-meso-porous carbon electrodes in ionic liquid based electrolytes. Tartu, 2022, 134 p.